Politecnico di Torino

Politecnico di Torino

Master's degree in Nanotechnologies for ICTs
A.a. 2022/2023

High performance wide-bandgap perovskite and semi-transparent solar cells manufactured by Flash Infrared Annealing

Relatori:
Prof. Fabrizio GIORGIS
Dr. Sandy SANCHEZ ALONSO

Candidati:
Giovanni RUFFOLO

Contents

Abstract

Single-junction and multi-junction (tandem) perovskite solar cells represent in today's PV field one of the most investigated technologies. The promising results reached during the past two decades lead to efficiencies up to 26.1 % for single-junction and up to 33.7 % for perovskite/silicon tandem solar cells higher than the widely diffused single-junction silicon solar cells. Nevertheless, the market share of PV is still dominated by the well-established silicon technology since organic-inorganic perovskites are sensitive to atmospheric environmental conditions, such as exposure to moisture. The lab-scale perovskite processing methods typically employed are challenging to scale up and not environmentally friendly due, among other reasons, to the high amount of harmful solutions they exploit. In this scenario, Flash InfraRed Annealing (FIRA) represents a promising alternative to avoid toxic solvents and prolonged annealing times incurring high energy consumption. This photonic annealing method enables the crystallization of pinhole-free perovskite thin films with an irradiation time of less than 1 second and yields single-junction solar cell efficiencies of up to 20%.

The goal of this thesis work is to realize an efficient and stable wide-bandgap perovskite solar cell for multi-junction devices using FIRA processing. To carry out the envisioned project, the composition of the deposited organic-inorganic hybrid perovskite thin films was adjusted to achieve an optimal optical bandgap and obtain devices with satisfactory performance. Different anionic and cationic stoichiometries were tested in the solution precursor to identify the best candidate to manufacture perovskite halide solar cell devices. The results showed that FIRA could be successfully applied to realize thin films with different iodine-bromine ratios with EQE comparable to the already optimized FAPbI3 composition. Instead, chlorine-containing films showed a less performant behavior than the iodine-bromine counterpart. Indeed, the presence of chlorine seems to be leading to phase segregation phenomena that hinder the quality of the grown layers. Devices were characterized using different spectroscopy techniques, optical and electron microscopy, morphological surface analyses, and typical solar cell characterization methods (JV, EQE). Lastly, the electrode responsible for hole extraction was optically optimized by realizing a highly transparent dielectric/metal/dielectric stack. This optimization would allow the non-absorbed radiation by the active area of the top cell to reach the bottom cell in a multijunction structure.

Introduction

The energy issue

The economy of most of the countries around the world is based on the harvesting and storage of energy in different forms. For historical and commercial reasons, together with the Joule (J) [1], other units have been introduced as the tonne of oil equivalent (toe) to quantify the oil fuel supplies, and the the kilo Watt hour (kWh) (3.6×10^6 J) employed at commercial level to quantify the electrical energy [2]. The need to introduce these large units is itself a proof of the large amount of energy used by humans for their activities. According to the International Energy Agency (IEA), in 1990 the amount of electricity consumed in the world was 10894.7 TWh and reached the value of 24901.4 TWh in 2020 [3]. These data show how the need of this form of energy is increasing over the years. Figure 2.1 shows the evolution of the global energy consumption by source over the last 32 years. From this chart is clear that we still rely on fossil fuels as primary energy resource. To accomplish the target of limiting the global warming to 1.5°C, greenhouse gas emissions must peak before 2025 at the latest and decline 43% by 2030 according to the results of the Paris agreements of 2015 [4]. In this scenario, solar energy represents one of the main *green* solutions exploited and studied today. Its development can be a key to reduce our dependence on fossil fuels.

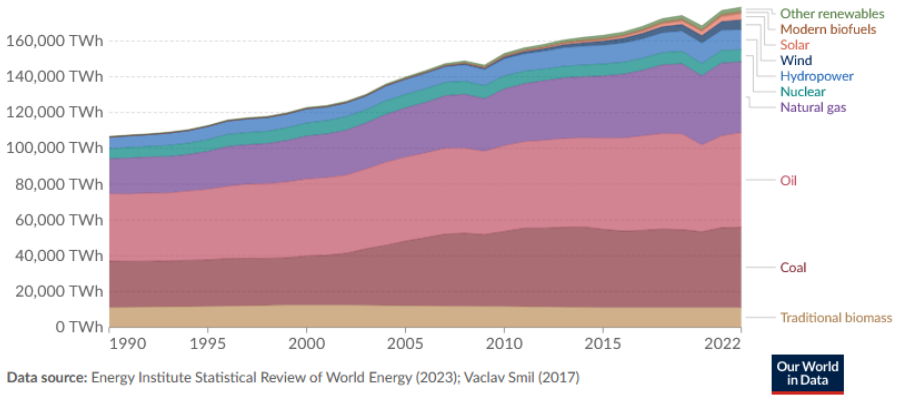

Figure 2.1. Chart of the global energy consumption by source. Nowadays, we still rely in fossil fuels as primary energy resource. Energy from solar represents only a small portion of the total energy consumed. Sources: *Our World In Data* and Energy Institute Statistical Review of World Energy (2023) [5].

New concepts of solar cells

The single junction solar cell made of crystalline silicon is the photovoltaic technology that dominates the market today. This structure belongs to the so called "first generation", where solar cells are realized on silicon wafers [6]. In figure 2.2b is shown a table of the market share of the solar cell technologies up to 2030. According to the previsions [7, 8], newer cells' generations characterized by thinner structures, flexibility and based on new physical concepts will make inroads in the market. Crystalline silicon solar cells are typically 200-300 μm thick, while thin-film solar cells, that belong to the "second generation", have a thickness of the order of few microns. Therefore, smaller cost is guaranteed since less material is needed for the same exposed cell's area. Figure 2.2a shows that thin-film technology reached the market, especially for flexible applications. But the performance of these solar technologies are not higher than the first generation of solar cells. A different trend is revealed by the "third generation" where the target is to achieve both high efficiency and low cost [6]. To this category belong for instance dye-sensitized solar cells (DSSCs), quantum dot-sensitized solar cells (QDSSCs), organic solar cells, and hybrid perovskite solar cells. Some of these concepts have already overcome the theoretical limiting efficiency of the single junction cell of 31% at *1 sun* illumination. This happened thanks to the *tandem* (or *multijunction*) solar cells (TSCs) structure where multiple junctions are exploited and each of them is responsible of absorbing a certain portion of the solar spectrum [6,9]. Under 1 sun irradiance, the theoretical efficiency for two junctions (2J), three junctions (3J) and infinite number of junctions are 46%, 50%, and 65%, respectively, by assuming 100% radiative emission and considering both solar irradiance and electroluminescence of the other sub-cells [10]. In figure 2.3 is shown the state of the art and evolution of the various photovoltaic (PV) technologies with their efficiency [11]. Whilst c-Si PV remains the cheapest way to produce solar electricity, they are approaching their theoretical maximum efficiency with only minor improvements in the past few years [12]. Perovskite solar cells have shown promising results during the past years and they can represent a valid alternative to silicon thanks to the advantages related to thin film PV technology.

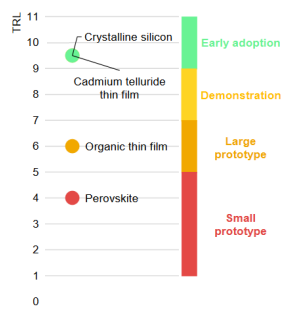

(a)

Technology		2014	2020	2030
Silicon-based (c-Si)	Monocrystalline	92%	73.3%	44.8%
	Poly- or multicrystalline			
	Ribbon			
	a-Si (amorph/micromorph)			
Thin-film based	Copper indium gallium (di)selenide (CIGS)	2%	5.2%	6.4%
	Cadmium telluride (CdTe)	5%	5.2%	4.7%
Other	Concentrating solar PV (CPV)	1%	1.2%	0.6%
	Organic PV/dye-sensitised cells (OPV)		5.8%	8.7%
	Crystalline silicon (advanced c-Si)		8.7%	25.6%
	CIGS alternatives, heavy metals (e.g. perovskite), advanced III-V		0.6%	9.3%

(b)

Figure 2.2. **(a)** Level of commercialization [7] and **(b)** market share predictions for different PV technologies [8].

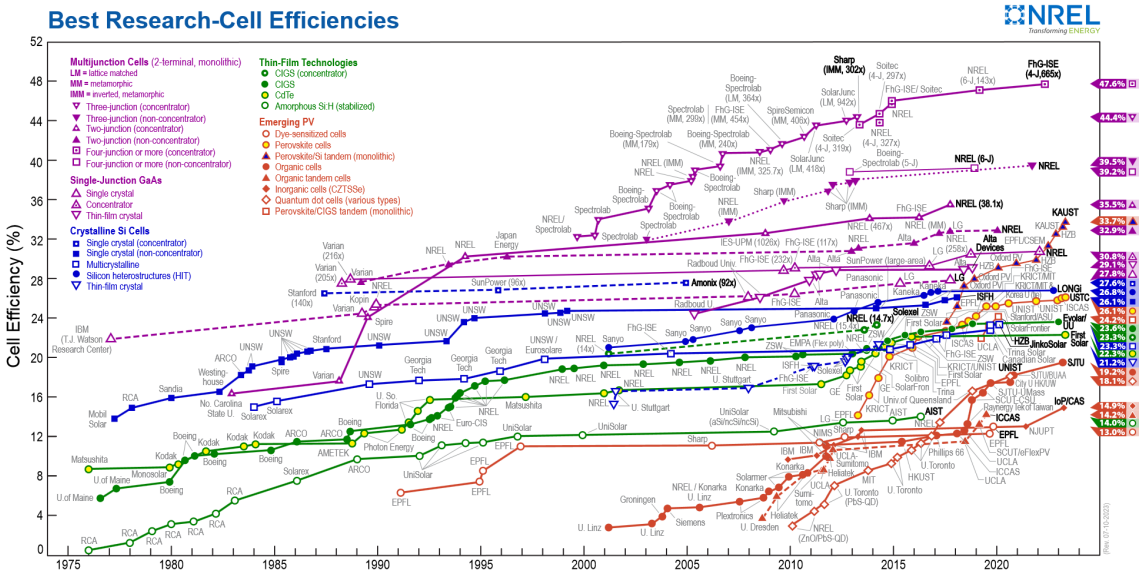

Figure 2.3. Best efficiency chart released by the National Renewable Energy Laboratory [11].

2.1 Working mechanisms of solar cells

The solar cell is the basic unit of a solar module (figure 2.4) and it allows to directly convert the energy of the light into electricity. The incident photons generate charge carriers that are moved by an electromotive force toward an external load. Once the carriers are generated, these must be extracted through the electrodes that should guarantee a small series resistance and high transparency to not hinder the light on reaching the active part of the device. Indeed, the photocarriers should be generated in the active region of the cell where charge extraction is effective [13]. Different concepts of solar cells have been studied and developed since the past century, some reached the commercialization, others are studied at laboratory level. To well understand in details their working principles an introduction to the physics behind solar cells is going to be depicted in the following paragraphs. This description will comprise the physics of semiconductors, electromagnetic waves, and their interaction. After, the discussion will move toward the integration of perovskites in solar cells and why they represent a strong candidate in the future of photovoltaic [14].

The electromagnetic spectrum

Photons are particles of light. Specifically, they have both wave-like and particle-like properties and each photon has a specific energy, E, given by the *Planck's law*:

$$E = h\nu \tag{2.1}$$

where h is the *Planck's constant* (4.14×10^{-15} eV·s) and ν is the *frequency* of oscillation of the photon expressed in s^{-1} or Hertz (Hz). The energy can also be related to the *wavelength* λ of the photon through the relation $E = hc/\lambda$. According to the quantum theory, light is quantised and only specific values of energy are admitted [16, 17]. Photons move with

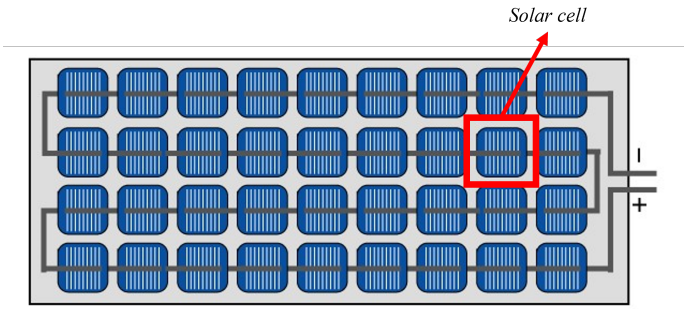

Figure 2.4. An example of a photovoltaic module composed of 36 solar cells connected in series. Image adapted from [15].

a velocity that depend on the refractive index n of the medium according to the formula $c = c_0/n$ where $c_0 = 2.998$ x 10^8 m/s is the photon's speed in vacuum. The wave-like behavior is generally invoked to describe diffraction and interference phenomena, while, the particle-like property is used to describe quantum-like energy transport. *Electromagnetic waves* can be described in terms of the electric and magnetic fields or, according to quantum mechanics, as a set of photons traveling with the speed of light c [16, 18]. In figure 2.5a is represented the so called electromagnetic spectrum where the different bands have assigned their commonly employed names.

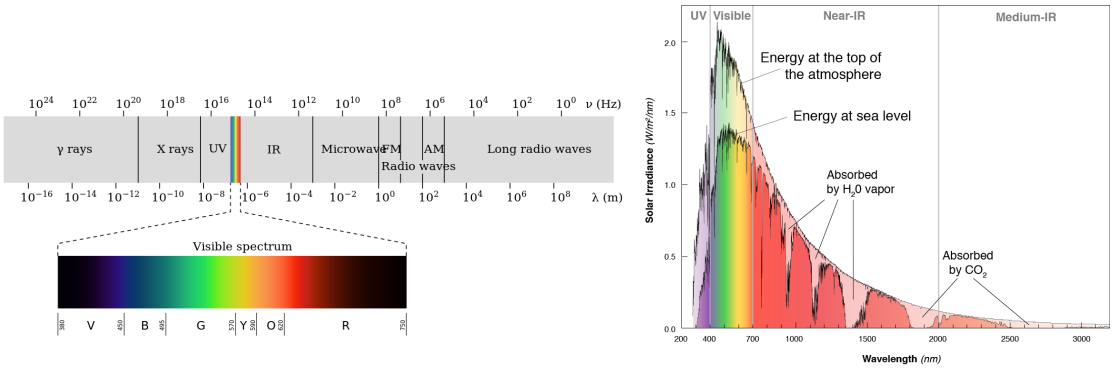

(a) **(b)**

Figure 2.5. **(a)** The electromagnetic spectrum with the corresponding commonly used name for each interval of wavelength (λ) in meters and frequency (ν) in Hz. The visible portion is highlighted. **(b)** The solar spectra of the light that reaches the top of the atmosphere (transparent plot) and the bottom of the atmosphere. Images' source: *Wikimedia Common*.

Solar spectrum and Air Mass

When we refer to the "amount" of light that illuminates a surface, a physical quantity named *Irradiance*, I_λ, is employed. It is defined as a flux density of photons or, in other words, the average energy per unit area per unit time expressed in $W\ m^{-2}$. Usually, to show how the irradiance emitted by the sun changes with respect to the wavelength, the solar irradiance per wavelength interval, E_λ, is represented. E_λ is known as *Spectral Irradiance*, expressed in

$W\ m^{-2}\ nm^{-1}$, and derived from: $E_\lambda = dI_\lambda/d\lambda$. For instance, in figure 2.5b, a plot of E_λ for different wavelengths that reaches the Earth at the top and bottom of the atmosphere is shown. This plot known as *Solar spectrum* has a maximum at 500 nm, corresponding to a photon energy of 2.48 eV.
Some of the solar radiation is absorbed while reaching the Earth's surface. It is a consequence of gases such as water vapor (H_2O), carbon dioxide (CO_2), and so on, as well as by dust, ozone, and oxygen that are strong absorbers in the infrared (IR) range and contained in the atmosphere. This is the reason why in 2.5b, some "holes" are present in the solar spectrum in the IR portion. Such absorption increases with the length of the path through the atmosphere and therefore with the mass of air across which the radiation passes through. The path length l traveled by a radiation from the Sun through the atmosphere is given by

$$l = \frac{l_0}{cos\alpha} \tag{2.2}$$

where α is the light ray incident angle relative to the normal to Earth's surface and l_0 is the thickness of the atmosphere. The ratio l/l_0 is called *air-mass* (AM) coefficient. AM is used to characterize the real solar spectrum after the absorption of a layer of air. The spectrum outside the atmosphere is designed as AM0, while on the surface of the Earth at a normal incident angle is the AM1. The spectrum used to measure the solar cells' efficiency for terrestrial applications is the AM1.5, a typical spectrum for moderate climates and corresponds to an angle of incidence of $\alpha = 48°$. By integrating the area subtended by the AM1.5 spectrum of 2.5b, the AM1.5 irradiance is obtained: $I_{\lambda,AM1.5} = 1000\ \mathrm{W{\cdot}m^{-2}}$. While, the irradiance outside the atmosphere has a value equal to $I_{\lambda,AM0} = 1353\ \mathrm{W{\cdot}m^{-2}}$. The difference between these two quantities gives an idea of how much the atmosphere contributes to attenuate the incoming power from the sun. Without it, we would be directly exposed to the sun's irradiation and the life on Earth would be impossible [16, 19].

2.1.1 Charge dynamics in solar cells

In a photovoltaic device, the active material should absorb the visible light, and use its energy to promote electrons lying in their initial occupied state of the material toward an higher unoccupied state. These two states have to be separated by an *energy gap* (or *band gap*) E_g. Such energy splitting is necessary because it allows excited electrons to remain in higher energy levels for a time long enough to exploit the gained potential energy as electrical energy. The only materials that posses an energy gap are *semiconductors* and *insulators*. Not *metals*, where there is a continuum of energy levels [20].
In figure 2.6 is shown the *valence band* (in orange) and *conduction band* (in blue) for three categories of materials: metals, semiconductors and insulators. In the conduction band are located all the electrons that have gained an high enough energy that can be used for electrical conduction. In metals the valence and conduction bands overlap. Instead, in semiconductors and insulators they are separated by the energy gap. Therefore, electrons need to overcome this energetic barrier E_g to be exploited for electrical conduction [16, 21]. What are the reasons behind these distinct electrical properties for these different materials?

The quantum nature of matter

From the quantum theory, when electrons are bound to the nucleus of the atom, they can lie only in specific energy levels that can be $1s^1$, $1s^2$, $2s^1$, ... states. The occupation of these states follow the Pauli exclusion principle for particles with a non-integer spin and it states that can never be more than one particle in the same quantum state. Since electrons can assume a spin equal to either -1/2 or 1/2, this rule must be accomplished. Therefore, we can observe that matter is quantized, and only certain specific energies are allowed. The energy difference between allowed levels depends on several factors: from the nature of the considered isolated atom, to the type of interactions that exists between neighbouring atoms. Indeed, when atoms form bonds, this quantization is affected especially for the outer electrons called *valence electrons*. These are located in the highest available state, and are directly involved in bondings with the surrounding atoms. A *monovalent* atom has only one valence electron available to form bonds, while a *divalent* one has two, and so on. Instead, the electrons in the lower levels of an atom, the *core electrons*, do not participate to the formation of bonds.

Conduction in Metals

Figure 2.7a shows how the outer states broaden while the number of atoms in close proximity increases. In this example, only a single *3s* energy level is available in the isolated atom. When the number of atom in close proximity rises, the contribution to the *3s* energy band increases and new slightly energetically different levels (or states) can be occupied. This process lead to the formation of a continuous band. In metals, the density of available states is so high, that the filled valence band (in 2.7a formed by $3s$ levels) interpenetrates with the partially empty conduction band ($3p$ levels). As a consequence, a small amount of energy is enough to excite an electron from an occupied state toward an higher unoccupied one. This happens in metallic solids where the atoms are arranged in a crystal structure and that can assume different configurations e.g. Face-Centered Cubic (FCC) and Body-Centered Cubic (BCC). The atoms in the solid metal are so close that their valence electrons orbitals interpenetrate each other. Instead, all the core orbitals that are closely bound to the nucleus do not form bands and do not contribute with their electrons to the electrical conduction process. Instead, the electrons in higher states can be used for current conduction and belong to a *sea of electrons*, or *Fermi sea*. As depicted in figure 2.7b, all the atoms that constitute metallic bonds contribute with their valence electrons to this sea where charges are delocalized and move freely without belonging to a specific atom. This is what happens in metals as

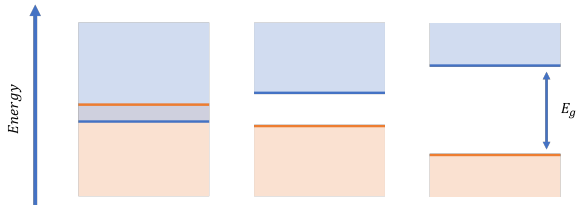

Figure 2.6. From the left to the right, the energy-band diagram for a metal, a semiconductor, and an insulator.

silver and gold that have an half-filled outer s band [21]. Thanks to the presence of this Fermi sea, metals have an electrical conductivity higher with respects to the non-metals.

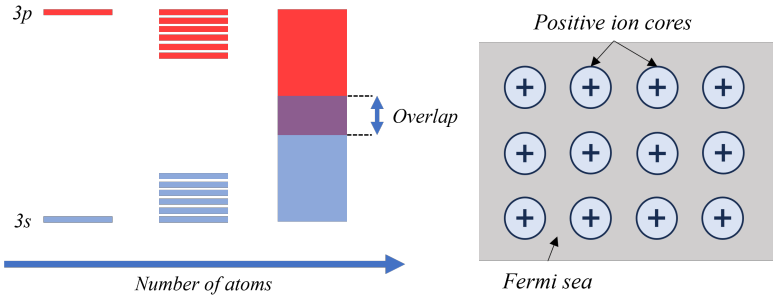

Figure 2.7. **(a)** In an aluminum atom the 3s level is fully populated, while the 3p is only partially. By increasing the number of bonded atoms, the 3s and 3p levels broadens into energy bands up to an overlap between the two. This makes electrons in the valence band available for conduction without the need to jump an energy gap. **(b)** The positive ion cores are surrounded by a sea of electrons in a metal.

Carrier dynamics in Semiconductors

In *insulators*, electrons are bound to the bonding atom by *ionic* or *covalent bonding*. Ionic bondings are observed between atoms with large differences in terms of *electronegativity*, a quantity that indicates the degree by which atoms attract electrons to themselves. The atom with lower electronegativity loses an electron and forms a *cation* X^+ (where X is the element). As a consequence, due to the stronger attraction between the negative electronic cloud and the positive nucleus, the atomic size decreases. The electron lost by the cation is gained by the atom with higher electronegativity that forms an *anion* X^-. In this case the atomic radius increases. In covalent bonds, the electronegativity difference is smaller (above 2.1 in ionic and below 1.5 in covalent). The nucleus of one atom attracts the electron cloud of the other, and when they are close enough, they form a bond by sharing their electrons. Both complete their outer electronic structure and they reach the lowest state of energy. Being strong, covalent and ionic bonds make electrons in insulators strongly bound to their bonding atoms. Therefore, they are not free to conduct and a lot of is needed to have conduction. This makes the E_g wide in insulators (see figure 2.6) which may be as much as 6 to 7 eV in pure diamond. In *semiconductors*, the difference in electronegativity between atoms is lower compared to insulator. This makes the gap E_g lower (e.g. 1.2 eV for silicon) and less energy is needed to promote electrons in conduction band. For this reason, semiconductors have electrical conductive properties intermediate between insulators and metals [21].

Generally, when a material possess thermal energy, this is contained almost entirely in form of random oscillations of the atoms around their rest position. These oscillations are quantized, as well as photons and electrons in matter, and the name of these vibrational quanta is *phonon*. Phonon energies ranges from 0 to 0.05 eV. When a photon is absorbed by the

material, an electron is excited toward an higher energetic state. In order to absorb a photon of any arbitrary energy, a continuous range of excitation energies must be available to the electrons. This is exactly what happens in metals when their surface reflectivity is reduced. After the excitation, the electron decays toward lowers levels step by step by emitting phonons. This process is called *thermalization* and takes places in times of the order of 10^{-12} s. In figure 2.8a is shown a scheme of how the excitation and the subsequent relaxation of an electron in a metal evolves with the absorption of a photon and emission of phonons. The same mechanism is shown in figure 2.8b for semiconductors. Here, we have a different behavior due to the presence of the energy gap E_g. First, the photon must provide an energy high enough to overcome the gap. This means $h\nu > E_g$. Otherwise, the photons will be transmitted or reflected. Once the electron goes in the conduction band, it leaves in the valence band a *hole*, a quasi-particle that has a positive charge. The promoted electron decays step-wise toward the minimum E_c by generating phonons. A further decay would require a release of an energy step equal to the bandgap that is higher than the single phonon energy. Indeed, this relaxation leads most of the time to the re-emission of a photon. Since this process, is much less probable than the emission of a single phonon, electrons may remain in the conduction band up to 10^{-3} s. These relatively long time allows the process of conversion of the electron energy into electrical energy as it happens in solar cells [16].

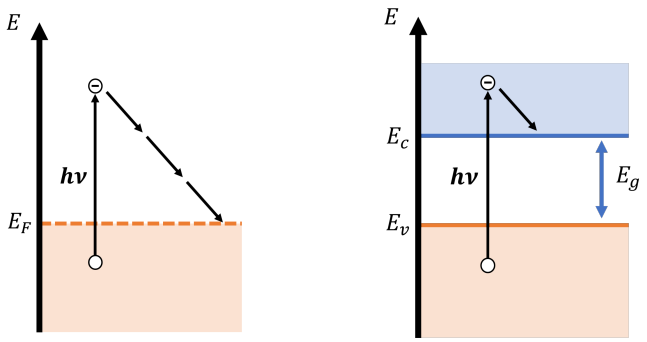

(a) **(b)**

Figure 2.8. **(a)** The excitation of an electron in the conduction band of a metal after the absorption of a photon with energy $h\nu$. The electron then decays toward the Fermi level E_F by emitting phonons. **(b)** The excitation of an electron from the valence band toward the conduction band in a semiconductor after the absorption of a photon $h\nu$.

For solar cells, the generation of electron-hole pairs as a consequence of the absorption of a photon is the most important process. The probability of a photon absorption is defined by a quantity called *absorption coefficient* $\alpha(h\nu)$. It depends on the material properties and not on the geometry of the absorber. Since absorption requires the availability of electrons for promotion and a partially occupied upper band, it is important to understand the population of the carriers in the involved bands. The distribution function which defines the occupation of the electron states is described through the *Fermi distribution*:

$$f_e(E_e) = \frac{1}{exp[(E_e - E_F)/k_B T] + 1} \tag{2.3}$$

where T is the temperature, k_B is the Boltzmann constant equal to 8.62×10^{-5} eV/K, E_e is the electron energy, and E_F is the Fermi energy. For states with $E_e << E_F$, $f_e(E_e) \approx 1$, so that the states are completely occupied. On the other hand, for $f_e(E_e >> E_F) \approx 0$ and the states with $E_e >> E_F$ are not occupied. Close to the edge of the band, electrons are treated like free particles with momentum p_e and mass m_e^* with an energy-momentum relationship (or *dispersion relation*)

$$E_e - E_c = \frac{p_e^2}{2m_e^*} \tag{2.4}$$

In figure 2.9a is shown the $E_e(p_e)$ relationship for a *direct-bandgap semiconductor* close to its band edges. In these class of semiconductors, the excitation of an electron from the valence band to the conduction band with the smallest possible energy, $E_c - E_v = E_g$, occurs without a change in momentum. Therefore, in this case we talk about *direct transitions*. Materials with this characteristics are GaAs, InP, and also cubic phase $FAPbI_3$ (Formamidinium lead iodide), an organic perovskite compound. When the conduction band minimum and valence band maximum are at different momenta, we have an *indirect semiconductor* with a band structure as the one shown in 2.9b. Indeed, the dispersion relations is:

$$E_e - E_c = \frac{(p_e - p_{e,0})^2}{2m_e^*} \tag{2.5}$$

The excitation from the maximum of the valence band to the minimum of the conduction band is only possible with a change in momentum. Materials with this property are for instance silicon (Si) and germanium (Ge) [16].

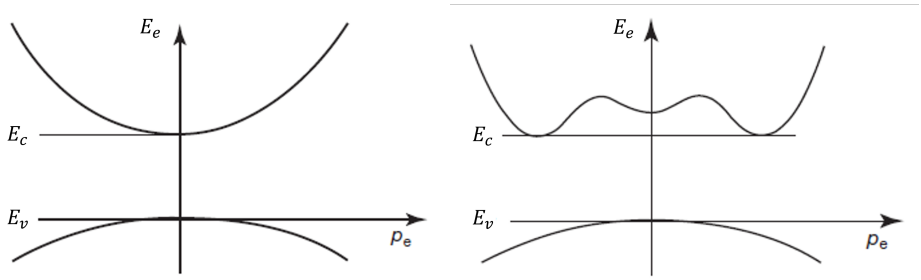

(a) **(b)**

Figure 2.9. **(a)** Band structure (E_e vs p_e) for a direct bandgap semiconductor. Here, the minimum of the conduction band and the maximum of the valence band occur at the same momentum $p_e = 0$ **(b)** Band structure of an indirect bandgap semiconductor. In this case the minimum and maximum are at different values of p_e. Images adapted from [16].

To study how the conduction band minimum and valence band maximum evolve along a device composed by different junctions, the *band diagram* is usually shown. Here the band edges are always shown. $E_c(x)$ and $E_v(x)$, as a function of one spatial direction (e.g. x). This representation gives no information on the momentum dependence of the band structure, and does not tell us whether the band gap is direct or indirect [20].

Generation and recombination of electron-hole pairs in semiconductors

In a semiconductor, the number of carriers of each type (electrons and holes) must be conserved. For a semiconductor containing electrons and holes, their conservation principle requires that:

$$\frac{\partial n}{\partial t} = \frac{1}{q}\nabla J_n + G_n - U_n \tag{2.6}$$

$$\frac{\partial p}{\partial t} = -\frac{1}{q}\nabla J_p + G_p - U_p \tag{2.7}$$

where $G_{n/p}$ is the volume rate of generation of electrons (holes) and $U_{n/p}$ is the volume rate of recombination. n and p are respectively the free electron and hole populations in the two bands. Generation is an electronic excitation event which increases the number of free carriers available to carry charge. Recombination is an electronic relaxation event which reduces the number of free carriers. Generation requires an input of energy while recombination releases energy. The energy input can be provided e.g. by light (photons). When an electron recombines, its energy can be released in different ways: by releasing a photon (*radiative recombination*), as heat through phonon emission (*non-radiative recombination*) or as kinetic energy to another free carrier (Auger recombination). In figure 2.10 these recombination phenomena are represented.

Photogeneration is the generation of mobile electrons and holes through the absorption of light in the semiconductor. It is the most important generation process in PV. The photogeneration rate can be described in terms of the absorption coefficient $\alpha(E)$ through the Beer-Lambert law:

$$I(x) = I(0)e^{-\alpha x} \tag{2.8}$$

where x is the distance along the material and $I(0)$ is the light intensity normally impinging the top of the surface of the absorbing material. Therefore, the light intensity decreases exponentially within the material since most of the photons are being absorbed in the medium.

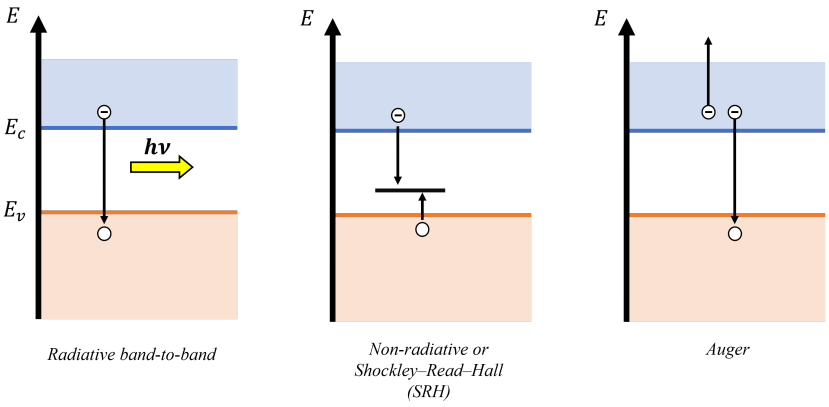

Figure 2.10. A simplified scheme of the working principle of the recombination processes in semiconductors.

Another parameter fundamental to have an efficient solar cell is the *diffusion length* for electrons and holes:

$$L_{n,p} = \sqrt{\tau_{n,p} D_{n,p}} \tag{2.9}$$

where $D_{n,p}$ is the diffusivity of the electron/hole and $\tau_{n,p}$ is the electron/hole carrier's lifetime. $L_{n,p}$ says how far the free carrier can move within the material before being recombined. In a good solar cell, the diffusion length must be larger than the characteristic dimension of the device to allow the free carrier collection at the electrodes [20]

Excitons

In the description above, electrons and holes states are treated independently. The Coulombic interaction between electrons and holes gives rise to hydrogen-atom-like states called *excitons*. These excitonic states are built up from the combination of electron and hole of same momentum. Excitons may be stationary (no momentum) or mobile along the semiconductor and they are electrically neutral. Their energy is defined by the following formula:

$$E_{exc} = \frac{m_{red} e^4}{2(4\pi\epsilon\epsilon_0)^2\hbar^2} \tag{2.10}$$

with $m_{red} = m_e^* m_h^*/(m_e^* + m_h^*)$ the *reduced mass*. In inorganic semiconductors, the binding energy of excitons defined by 2.10 is in the order of few meV because of the large permittivity ϵ. Therefore lower than $k_B T$ at room temperature. As a consequence, excitons exist in inorganic semiconductors only at low temperatures, and at room temperature, electrons and holes are free to move after being generated by the absorption of a photon. In organic semiconductors molecules are weakly bound by Van der Waals forces. This causes smaller dielectric permittivity and consequently higher binding energies for excitons in the order of some tenths of eV, much larger than $k_B T$ at room temperature. Even if electrons are excited toward energies higher than the binding energy of excitons, they may quickly be trapped back to the mutual attraction with holes and form an exciton.
In organic semiconductors at room temperature, the minimum energy of a free electron–hole pair, defining the free-carrier band gap, is larger than the optical band gap by the binding energy of the exciton. The excitonic levels are represented on band diagrams as a series of levels below the conduction band edge. Indeed, excitons lead to narrow lines in spectral analyses as optical absorption or photoluminescence spectra with energies below the energy gap of a semiconductor [16, 20, 22].

2.1.2 Electrical and Optical parameters

The solar cell is modelled electrically as a current generator since the induced current flow is independent of the load. This current depends exclusively on the illuminating source characterized by a certain intensity and spectrum that was analysed in paragraph 2.1. Under dark condition, the cell does not drive any current into the circuit and behaves as a passive element. When light is switched on, an e.m.f. (electromotive force) is developed and a flow of carriers is detected at the load. When the working solar cell is short circuited the *short circuit current* I_{sc} is derived. Instead, when the two terminals of the cell have no load connected, the *open circuit voltage* V_{oc} is obtained. These two electrical quantities are fundamental to describe electrically a solar cell since they allow to derive important figure of merits employed at commercial level to quantify the performance of the cell. [16].

Short circuit current and Quantum Efficiency of a solar cell

The photocurrent is the current generated as a consequence of the illumination. If the load has a resistance $R = 0\,\Omega$, an I_{sc} is obtained. This quantity corresponds to the maximum current that can be drawn from a solar cell and depends on the exposed area of the cell, the light spectrum, optical properties (reflection, absorption, and transmission), and carriers collection probability. To remove the dependence on the exposed area, and allow to compare different cells, the *short circuit photocurrent density* J_{sc} (in mA/cm^2) is commonly employed. Indeed, the photocurrent can be obtained back from .this realtion: I_{sc}=$J_{sc} \cdot A$, where A is the area of the cell. To relate the photocurrent density J_{sc} to the light spectrum, the following relation is considered:

$$J_{sc} = q \int I_\lambda(E) QE(E) dE \tag{2.11}$$

where q is the electronic charge [20]. The irradiance $I_\lambda(E)$ according to the Kirchhoff's Radiation Law is defined as $I_\lambda(E) = \epsilon_\lambda / \alpha_\lambda$. Therefore, it is related to the the abilities of a body to emit and absorb electromagnetic energy through the *emission coefficient* ϵ_λ and *absorption coefficient* α_λ. These two quantities depend on both the nature of the surface of the body (color, texture, etc.) and on which wavelengths the body emits or absorbs well [19]. The other quantity is the *Quantum Efficiency* QE and it represents the probability that an incident photon of energy E generates and deliver an electron-hole pair to the solar cell's load. QE depends on the absorption properties of the material, charge collection and separation capabilities of the cell, all intrinsic properties of the device itself [20]. Therefore, QE can be used to compare different devices independently from the solar spectrum.
In figure 2.11 are plotted two different types of QE. These are the *External Quantum Efficiency* (EQE) and the *Internal Quantum Efficiency* (IQE). The EQE gives information about how efficiently photons are converted into electron-hole pairs by the solar cell as a function of the wavelength. If the amount of photons reflected or transmitted is known, the IQE can be determined:

$$IQE(\lambda) = \frac{EQE(\lambda)}{(1 - R(\lambda)} \tag{2.12}$$

with $R(\lambda)$ being the reflectance. Thus, knowledge of the quantities EQE and IQE enables distinguishing the loss mechanisms due to nonoptimal optical absorption properties of the

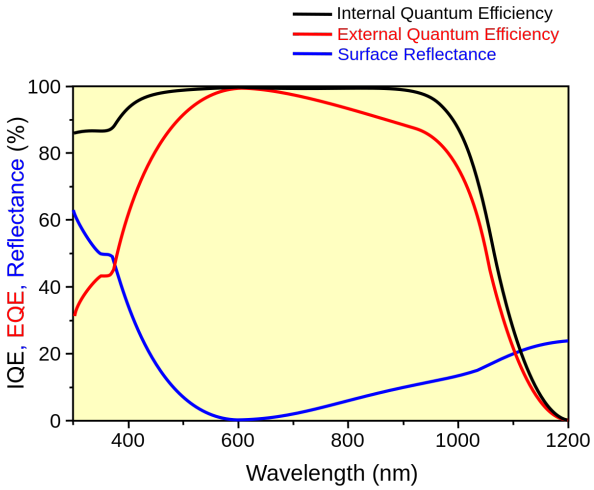

Figure 2.11. IQE, EQE and surface reflectance of a crystalline silicon solar cell with antireflective coating as a function of the incident wavelength. The plot has been calculated with *PC1D*. Image adapted from *Wikimedia Common*.

entire device from the photoconversion properties of the absorber [16].

Dark current and open circuit voltage

When the solar cell is connected to an external load, it develops a voltage drop between its terminals. This lead to the generation of a current named *dark current* $I_{dark}(V)$ whose direction is opposite to the one of the photocurrent. Most solar cells behave like a diode in the dark:

$$J_{dark}(V) = J_0(e^{qV_A/k_BT} - 1) \tag{2.13}$$

where J_0 is the reverse saturation current of a diode. Indeed by applying a forward bias V$_A$¿0, when V$_A$ goes above few k_BT/q volts, the exponential term dominates. While for a reverse bias V_A¡0, when the value k_BT/q is exceeded, the exponential term is neglected and the current-voltage relation is flattened toward a small value of dark current $J_{dark} = J_0$. Therefore, the system is behaving as a Schottky contact. The overall current-voltage response of the cell can be thus approximated by the sum of these two currents:

$$J(V) = J_{sc} + J_{dark}(V) = J_{sc} + J_0(e^{qV_A/k_BT} - 1) \tag{2.14}$$

for an ideal diode. In figure 2.12 is shown this behavior in dark (diode-like) and under illumination. Usually, to better visualize the I-V curve (or J-V curve), the negative part of the y-axis, that is the current, is shown on the top. When the contact are isolated and the potential drop across the cell reaches its maximum, the open circuit voltage V_{oc} is obtained. This is equivalent to the condition when the dark and photogenerated currents cancel out. From the ideal diode equation 2.13 the result is a logarithmic increasing V_{oc} with light intensity:

$$V_{oc} = \frac{k_BT}{q} ln\left(\frac{J_{sc}}{J_0} + 1\right) \tag{2.15}$$

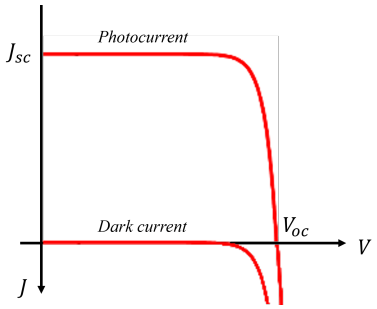

Figure 2.12. Current-voltage characteristic of an ideal diode under illumination and in dark. According to the approximation of 2.14, the photocurrent curve is obtained by shifting of J_{sc} the dark current curve.

From figure 2.12 the current-voltage product is negative in the visualized plot quarter. This means that the cell is generating power. This region of the current-voltage plot is called *photovoltaic region*.

Power conversion efficiency (PCE) and Fill Factor (FF)

The cell's voltage operational range is between 0 V and V_{oc}. The power that the cell can delivery within this rage is given by the product $P = VI$ (power density if we consider the current density J). As visible from figure 2.13a, the *maximum power point* is where the power reaches its maximum. Therefore, an optimal load should have a resistance given by the ratio V_{mp}/J_{mp}. The *fill factor* is defined as:

$$FF = \frac{J_{mp} \cdot V_{mp}}{J_{sc} \cdot V_{oc}} \tag{2.16}$$

This parameters describes the "squareness" of the J-V curve. Therefore, it is a useful measure of how much the cell is close to an ideal diode behavior. Another parameter used to quantify the efficiency of the cell and widely employed at commercial level is the *power conversion efficiency* PCE. It is defined as:

$$PCE = \frac{J_{mp}V_{mp}}{P_s} = \frac{J_{sc} \cdot V_{oc} \cdot FF}{P_{inc}} \tag{2.17}$$

where P_s is the incident power density. Therefore, the PCE can be related also to the FF. To measure all the above mentioned parameters, a *Standard Test Condition* is followed by using an irradiance corresponding to the AM1.5 spectrum, that means 1000 Wm^{-2} [16].

Parasitic resistances

In real solar cells, parasitic effects can arise for different reasons. In figure 2.14 is shown the one-diode equivalent circuit model for solar cells. It takes into account the parasitic effects through the *shunt resistance* R_s and the *series resistance* R_s. The series resistance is a consequence of the finite conductivity of the semiconducting material, contact resistance between the semiconductor and the adjacent electrodes, and the resistance associated with the electrodes and interconnections. The shunt resistance represents the loss of carriers via

possible leakage paths as structural defects or recombination centers introduced by impurities in the active material of the cell. In figure 2.13b, the consequences of the resistances on the current-voltage plot is highlighted. In the equivalent circuit, the diode allows the photovoltage drop that drives the photocurrent through the load. Once all these effects are taken into account, the equation 2.14 is re-written in the following form [16]:

$$J(V) = J_{sc} - J_{dark}(V) - J_{sh} = J_{sc} - I_0(e^{qV_A/k_BT} - 1) - \frac{V + JAR_s}{R_{sh}} \tag{2.18}$$

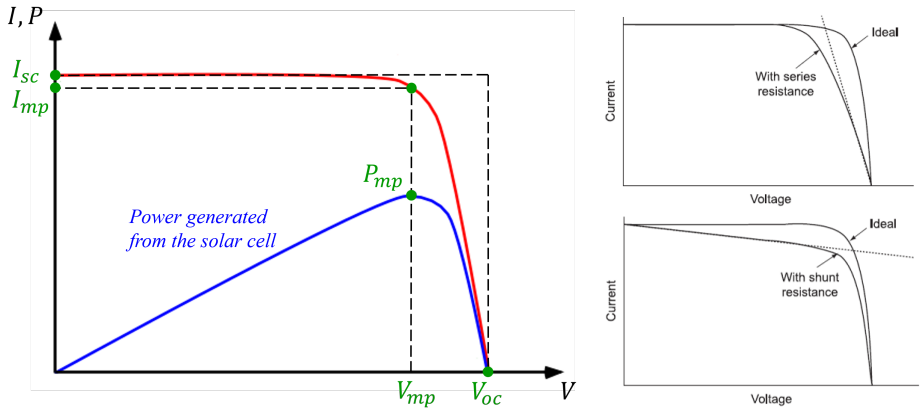

Figure 2.13. **(a)** Current-voltage and power-voltage characteristic for an ideal cell without parasitic resistances. The area of the inner rectangle obtained by the product $I_{mp}V_{mp}$ gives the maximum power density that can be delivered by the cell. The rectangle with area $I_{sc}V_{oc}$ would be the shape of the I-V curve if the solar cell had a FF equal to 1. **(b)** The effect of the series and shunt resistances to the I-V curve.

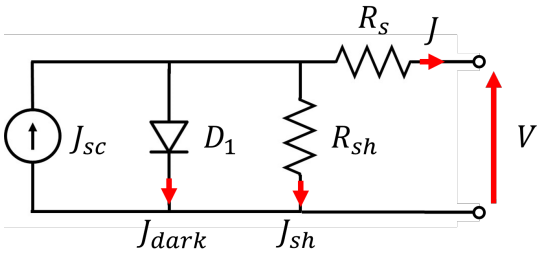

Figure 2.14. The equivalent circuit of a solar cell with the parasitic resistances.

2.2 Perovskites for photovoltaic applications

The application of perovskites to devices based on light-matter interactions has been investigated for many years. Applications such as light-emitting diodes have been reported by Chondroudis and Mitzi in 1999 [23]. Instead, the first application of perovskites as light absorbers traces back to 2009 when Akihiro Kojima and collegues in Japan applied lead halide perovkite compounds as active layer in dye-sensitized solar cells (DSSC) [24]. The research on perovskite-based photoabsorber materials is still in progress and during the years they are emerging as a promising alternative for cost-effective and solution processable photovoltaic (PV) devices. *Metal halide* perovskites offer several interesting semiconductor traits: direct tunable bandgaps, strong light absorption, long electron-hole diffusion lengths, and relatively small electron/hole effective masses. [25,26] During the work described in the following chapters, the bandgap tunability was exploited, specifically working with *hybrid organic-inorganic* perovskites whose anionic and cationic composition was tuned. This to target the maximum theoretical efficiency that can be reached for a perovskite-on-perovskite tandem solar cell according to the color map shown in figure 2.21.

2.2.1 Crystal structure of Perovskites

Discovered by Gustav Rose in 1839 and named after the mineralogist Lev Perovski, perovskites is a family of crystalline compounds that assume the crystalline structure of the $CaTiO_3$ (Calcium titanate) shown in figure 2.15b. In the perovskite ideal structure, the unit cell is FCC (Face centered cubic) and its periodicity in space lead to the formation of a 3D perovskite network visible in figure 2.15a with the typical octahedrical shape assumed by the X atoms. A and B are monovalent and diavelnt cations respectively, while X is the anion. Highly symmetric cubic structures show enhanced optoelectronic properties in perovskites, but the cubic structure is quite uncommon due to the differences in terms of dimensions of the constituting atoms. As a consequence, we usually have a structural distortion. [21,25]

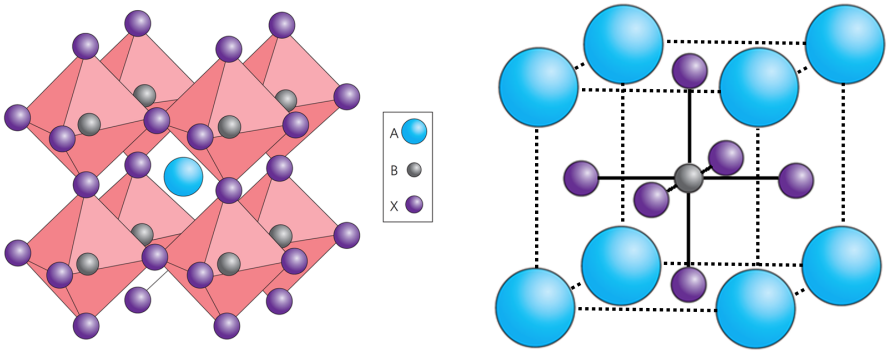

(a) **(b)**

Figure 2.15. **(a)** Cubic perovskite structure ABX_3 where each A-site cation is shared by 8 $[BX_6]$ octahedra [27]. **(b)** The $CaTiO_3$ crystal structure.

Perovskite tolerance and octahedral factors

A parameter that can be used to determine the degree of distortion from the cubic perovskite structure is the *Goldschmidt tolerance factor* that is defined as

$$t = \frac{r_A + r_X}{\sqrt{2}(r_B + r_X)} \tag{2.19}$$

Where r_A, r_B, and r_X are the ionic radii of the A, B, and X components of the perovskite lattice respectively. t = 1 corresponds to a perfectly packed cubic lattice and a stable cubic perovskite structure is still observable for $0.9 \leq t \leq 1$. Most perovskite composition have t between 0.8 and 0.9. For instance, when the A-site cation becomes too large ($t > 1$), non-perovskite structures as hexagonal structure are formed. The same happens for $t < 0.8$ when the A-site cation is too small to form a perovskite structure [25, 28] . The lattice evolution with the tolerance factor is shown in figure 2.16. Together with the Goldschmidt tolerance factor, another parameter helps on understanding the stability of the crystalline structure is the *Octahedral factor* that is defined as

$$\xi = \frac{r_B}{r_X} \tag{2.20}$$

It represents the structural stability of the BX_6 octahedron. A stable perovskite structure is generally obtained for $0.44 \leq \xi \leq 0.9$. Among the advantages related to the use of perovskites

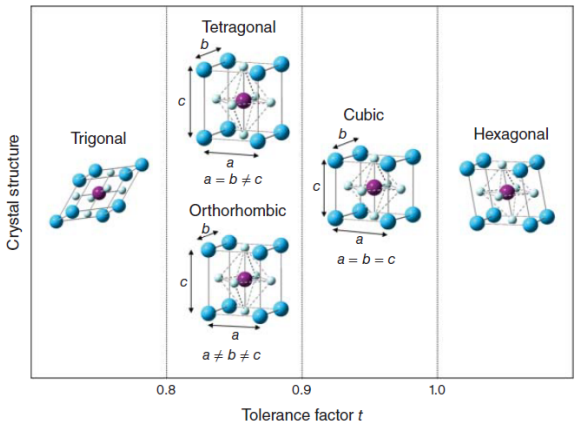

Figure 2.16. The crystal structure of perovskite and the corresponding tolerance factor. Image's source: [25].

in light harvesting applications, the possibility of tuning the optoelectronic properties of perovskite's thin films through compositional engineering represents a fundamental resource. Specifically, *hybrid organic-inorganic perovskites* have distinguished themselves as an efficient and inexpensive technology for solar cells applications [25].

2.2.2 A-site cation and X-site anion alloying

As mentioned before, a cubic packed perovskite structure is fundamental to obtain a well behaving 3D layer from both the optoelectronic and stability point of view. In figure 2.17

is shown the electronic structure of an ideal $APbX_3$. The valence band is built up by the s-orbitals of lead cation (Pb^+) and p-orbitals of lead and halogen ions (Cl^-, Br^-, and I^-). In this frame, the A-site cation does not contribute to the optoelectronic properties of the perovskite films. But, its shape, size, and charge distribution strongly affects the overall structural stability. For instance, the inorganic Pb–I framework is deformed by A-site cation through steric (spatial arrangement of atoms) and Coulomb interactions causing an octahedral tilting that changes the electronic structure near the band edges [25]. Another parameter

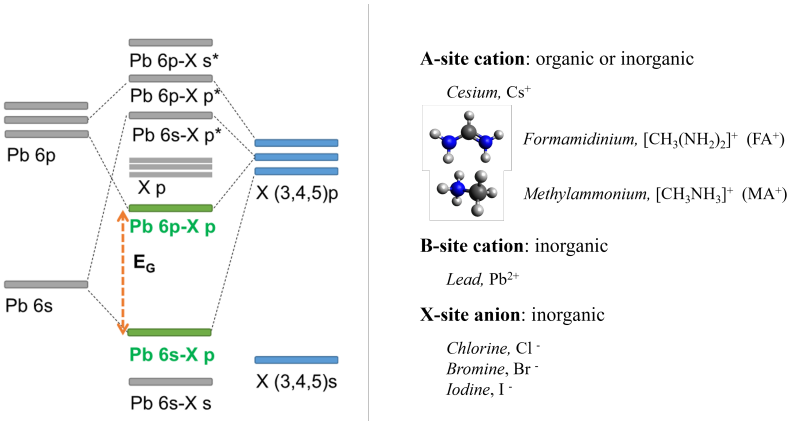

Figure 2.17. The electronic structure of the ideal $APbX_3$ perovskite. The valence band is build up by s (Pb) and p (X-site halide) orbitals while the conduction band consists of Pb and X-site halide p orbitals. On the right, the organic molecules and elements used in this thesis work as well as the most used in perovskite solar cells research. Image adapted from [29].

that must be considered to establish a stable cubic perovskite lattice is the *phase transition temperature*. Indeed, as temperature changes so do preferred lattice and phase configuration. The temperature threshold above which a perovskite cubic (α-phase) is assumed by the lattice depends on the sample synthesis, method, and history [30]. Usually, rich iodine perovskite compositions as $FAPbI_3$ have a phase transition temperature close to the room temperature. While, rich bromine compositions are typically cubic at room temperature. These structural changes can have drastic effects in the optoelectronic properties of perovskites. For instance, many non-cubic phases are photovoltaically inactive. To improve phase stability, perovskite alloying can be exploited: first by fixing the anionic composition to obtain the desired bandgap and, then, by selecting an appropriately sized mixture of A-site cations that satisfies the tolerance factors [31]. Incorporation of small ions as Cs^+ on the A-site of the $FAPbI_3$ or $MAPbI_3$ perovskites could lead to better thermal stability and photostability. For instance, in $Cs_{0.1}FA_{0.9}I_3$ the shrunken perovskite lattice is a consequence of the smaller cesium cations that reduce the cuboctahedral A-site vacancy and hence induce stronger interaction between A-site cation and iodide anions [25].
The advanced compositions of different A-site cations are prone to segregate due to the small differences in the formation energy of the available phases. This process can be explained in terms of the *Gibbs free energy* of mixing (ΔG_{mix}) that is the convertible energy due to phase

change. At constant pressure and volume ΔG_{mix} is defined as:

$$\Delta G_{mix} = \Delta H_{mix} - T\Delta S_{mix} \tag{2.21}$$

where ΔH_{mix} is the enthalpy of mixing calculated by taking the difference between the total energy of the mixed state and the initial reactants energy. $T\Delta S_{mix}$ is the entropy of mixing. Compositions with $\Delta G_{mix} < 0$ have components energetically favored to mix, causing them to form a shared single phase. On the other hand, compositions with $\Delta G_{mix} > 0$ are prone to phase segregate. Therefore, to make films which stay homogeneous during device operation, the mixed phase must be energetically favorable ($\Delta G_{mix} < 0$) to all the phases present at that temperature [31].

2.2.3 Perovskite solar cells

In order to drive out of the solar cell the current, electrons must flow out toward one electrode and the holes toward another one. To accomplish it, a material that has a high conductivity for electrons and low for holes can be deposited on one side of the active material. This selective layer is the *electron transport layer* (ETL) and behaves as an n-type material. The same selectivity is needed for holes. In this case we refer to an *hole transport layer* (HTL) where the hole conductivity is higher compared to electrons as in a p-type material. Perovskite solar cells (PCS) are realized according to these charge selection rules. In figure 2.18 are shown the most commonly employed structures for PCS and its working principle. By looking at the picture, (1) the perovskite absorber, undergoes photoexcitation by absorbing the photons whose energy is higher than the material's bandgap. (2) Then, electrons in the excited state (LUMO) of perovskite are injected into the conduction band of the ETL, while holes in the valence bad edge (HOMO) are injected in the HTL. (3) Finally, the electrons and holes are transported toward the corresponding electrodes. As visible in figure 2.18, a mesoporous ETL can be deposited on top of the compact ETL. TiO_2 is a commonly employed electron selective material deposited in compact and mesoporous layers. The role of the mesoporous material is to provide a large surface scaffold to accomodate perovskite crystals that enhances electron extraction, to increase the light path within the active layer through light scattering, and decrease the contact angle of the spin-coated perovskite solution on top of it [16, 32]. In figure 2.19 are shown some of the commonly employed materials in perovskite solar cells.

2.2.4 Tandem solar cells using metal halide perovskites

One of the main limit to the maximum efficiency of solar cells is the loss of energy in terms of thermalization (see figure 2.20) and the non-absorption of low-energy photons. The reduction of both these causes of losses can be accomplished by offering to the solar cell only photons within the narrow interval of the energies slightly above the value of the bandgap. This can be done by stacking several sub-cell where each of them is optimized with its bandgap to absorb one portion of wavelengths. By looking at figure 2.20, if the cell with the wider bandgap is placed so as it is the first to receive the electromagnetic spectrum, only the high energetic photons will be absorbed and the ones characterized by a smaller frequency are transmitted. The generated electrons in the first absorbing material are promoted close to the conduction

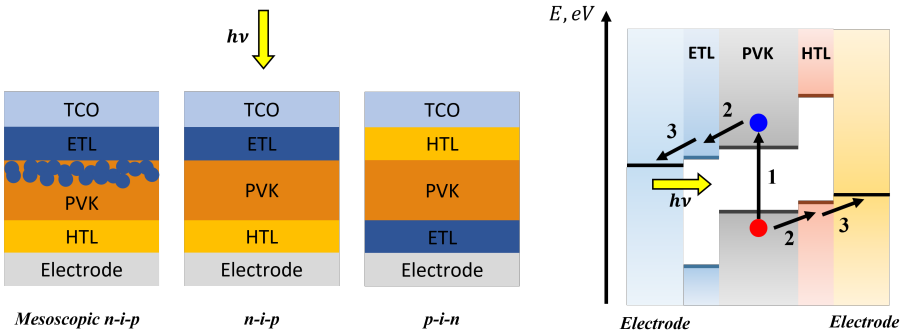

Figure 2.18. Generalized structure of a conventional mesoscopic n-i-p, planar n-i-p, and inverted p-i-n architecture. On the right, a schematic description of the electronic process in a perovskite solar cell.

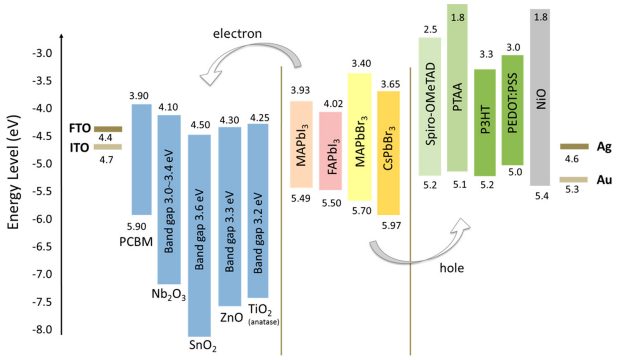

Figure 2.19. Here are shown some of the commonly employed electron selective materials, perovskite absorbers, and hole selective materials. Image source: [32].

band edge. Here they will not undergo thermalization and will stay at the edge for a time longer than the typical thermalization time that is $\approx 10^{-12}$ s. The transmitted light, will be absorbed by a successive absorbing material with a bandgap smaller than the previous one. This approach can be followed up to stacking several cells [16]. These type of structures are called multijunction or tandem solar cells. Perovskite-on-silicon and perovskite-on-perovskite (PVK-on-PVK) are two examples of double junctions tandem devices. For the PVK-on-PVK, the plots in figure 2.21 suggest which are the best bandgaps for both the bottom and top cell perovskite materials.

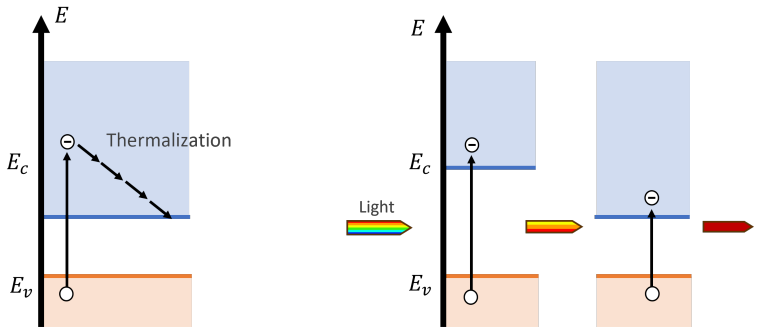

Figure 2.20. A simplified scheme of the working principle of tandem solar cells. The energy lost in terms of thermalization in the single junction cells is saved in a tandem structure where each sub-cell acts as a selective absorber for each wavelength range.

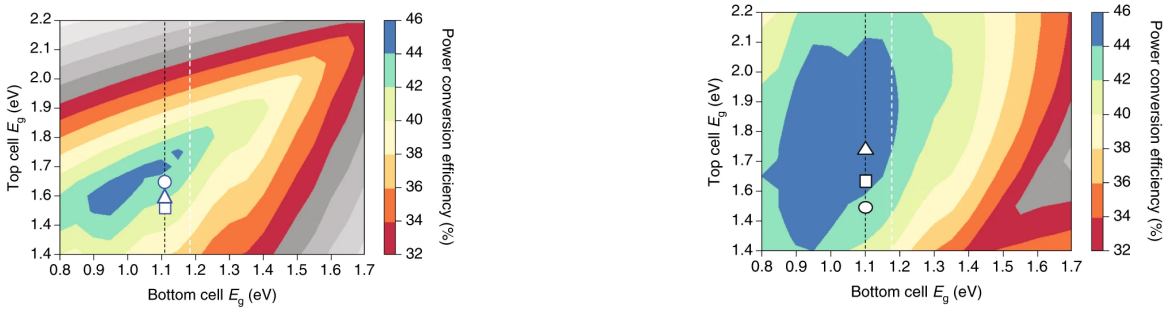

(a) **(b)**

Figure 2.21. **(a)** Theoretical efficiency limit for 2T tandems calculated considering optimal thickenesses of the two sub-cells. In the grey shading areas, there is no efficiency gain in building a tandem device. The dotted white lines mark the lowest bandgap currently accessible to metal halide perovskite semiconductors. The black dashed line marks the 1.12 eV bandgap of silicon, while the open symbols represent the bandgap combinations for the best-achieved 2T perovskite–Silicon tandems. In **(b)** is shown the same plot for the 4T configuration. Images adapted from [33].

2.3 Flash Infrared Annealing for perovskite processing

Scaling up the production of perovskite solar cells is one of the main challenges of this technology. All the perovskites compositions are soluble in water and this makes them sensible to environmental conditions (relative humidity more than 25%). As a consequence, lead halide perovskites tend to degrade. Moreover, most of the fabrication techniques currently employed are neither practical nor environmental friendly. For instance, the *antisolvent method* that is one of the most exploited and effective lab-scale method to induce perovskite's crystallization consumes a relative large amount of solvent (more than 50 μl/cm^2) and it is difficult to apply to large substrate's area (several square centimeters) [34]. In order to find a solution to this problem, a new synthesis method called *Flash Infrared Annealing* (FIRA) is introduced. Here, a rapid thermal process is executed and thin film layers of semiconductors that show micrometer-sized crystalline domains can be synthesized [35]. Rapid thermal annealing

processes have been successfully used to realize large inorganic semiconducting crystalline films e.g. for defect removal and doping activation in poly-crystalline silicon [36]. In 2015, Troughton et al. reported the first application to perovskite film synthesis with a photonic pulse of about 1 ms [37]. But in this study Al_2O_3 nanoparticles were added to the perovskite to allow the absorption of the infrared (IR) photons. Therefore, affecting the perovskite crystallization. In the following, the physicochemical phenomena that take place during the perovskite film crystallization with FIRA are introduced. The kinetics of the nucleation and crystal growth are also addressed.

2.3.1 Perovskite crystal nucleation and growth dynamics

The Antisolvent Dripping method

An antisolvent is a fluid that do not dissolve the solute but it is miscible with the solvent of the solution. When the antisolvent is added to a solution, it reduces the solubility and creates local supersaturation conditions. The consequence of this is the formation of precipitations and crystallization phenomena [38]. For perovskites, spin coating can be used as deposition method and then spread an antisolvent, typically a non-polar solvent as chlorobenzene, on the formed film. Being a very fast and a room temperature method, the Antisolvent Dripping method gained a lot of success in perovskite thin films growth. But the precision needed to deposit the antisolvent at the right time causes reproducible problems in terms of realized films [34].

Physics of Nucleation and Crystal growth

A nucleus can be defined as the minimum amount of a new phase. It is composed by few atoms or molecules from which the formation of a new layer develops. An initially metastable phase of nuclei is called nucleation, an extremely localized phenomenon that bring a sufficient number of atoms or molecules together to form a stable size. Then, a growth stage follows by the diffusion of particles, called growth units, to the surface of existing nuclei and their incorporation in the structure of the crystal lattice. In solution-processed perovskite materials, the perovskite layer is typically deposited by a solution coating method. When the so-called antisolvent is dropped on top of the spin-coated perovskite, a layer of solid perovskite growth. Then, thermal annealing follows to remove the remaining solvent and obtain a purer perovskite phase. As the solvent evaporates, the *chemical potential* of the solution changes. The chemical potential μ quantifies the tendency of the substance to change; that is to react with other substances, to transform into another state of aggregation. Therefore, with the variation of μ, supersaturation is eventually reached within the perovskite solution and the formation of a new crystalline phase is observed. Nucleation clusters appear once Gibbs energetic barriers are surpassed. This concept is highlighted in figure 2.22a. All the clusters of molecules that have radii less than the critical radius r_c will naturally tend to lower their energy by moving to the left of the curve and disappear by melting or evaporation. When the radius is larger than r_c, the cluster growths and increase its radius beyond r_c, thereby reducing the total energy. Therefore, the relationship between supersaturation and critical nucleus size inducing crystal growth can be represented in terms of Gibbs's free

energy of the system. The growth mode of a thin film can be described by the Young's equation at equilibrium:

$$\sigma_0 cos\theta = \sigma_2 - \sigma_1 \tag{2.22}$$

where θ is the contact angle the nucleus forms with the substrate, σ_0 the nucleus surface tension, σ_1 the nucleus–substrate interfacial tension, and σ_2 the substrate surface tension (see figure 2.22b). This expression can be used to derive the expression of the Gibbs's free energy per unit volume (ΔG_V) needed to go from an equilibrium state to supersaturation:

$$\Delta G_V = -Z(T) \cdot ln\frac{\rho_s}{\rho_e} = Z(T) \cdot ln(\xi + 1) \tag{2.23}$$

where $Z(T)$ is a coefficient depending on temperature and shape of the stable clusters, ρ_s is the concentration of supersaturation, and ρ_e is the equilibrium concentration. Also the change in surface and interfacial free energy can be derived:

$$\Delta G_S = \pi r^2 \sigma_0 (2 - 3cos\theta + cos^3\theta) \tag{2.24}$$

with r being the nucleation radius. From equations 2.22 and 2.23 the critical nucleus can be derived and its expression is the following:

$$r_c = \frac{2\sigma_0}{Z(T) \cdot ln(\xi + 1)} \tag{2.25}$$

The antisolvent method initiates the crystallization of the perovskite solution by changing its solubility. This leads to supersaturation and when this occurs, the balance of chemical potentials can surpass the nucleation barrier for certain nuclei sizes. The nucleation can be controlled by modulating the critical size, which is a function of the interfacial energy. The smaller the interfacial energy, the smaller the critical size as deducible from 2.24, and the more likely the nucleation becomes for any given supersaturation [34, 39].

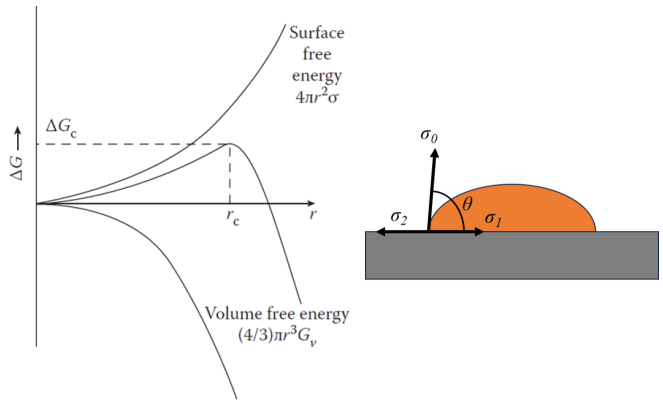

(a) **(b)**

Figure 2.22. **(a)** Change in free energy during the formation of a liquid droplet. Image from [39]. **(b)** A simplified sketch of the different forces involved in the Young's equation for a film growing on a substrate.

The Young's equation 2.22 can be used to predict the growth modes for surfaces grown by

PVD (Physical Vapor Deposition) techniques. When the contact angle $\theta \approx 0$, a layer by layer (or Frank – Van der Merve) growth is observed. Here, a new layer starts to build only if the bottom layer is completely formed. This growth mode lead to the highest crystal quality. When $\theta > 0$, the growth happens by the formation of islands (Vollmer–Weber growth) which will grow both laterally and vertically before they merge. This mode typically lead to more defective lattices, but their growth speed is higher compared to the layer by layer growth [40].

2.3.2 The FIRA method

Crystal growth kinetics is a complex phenomenon, which usually takes place through an intermediate phase. Overall, fast nucleation can improve the coverage of films, and the control of the crystal growth can contribute to form a high-crystalline material. To growth a crystal, the cluster is transported on the surface and then reacts with it. This transport is controlled by diffusion. Therefore, it can be driven by an energetic gradient in the system. In general, short-time annealing at high temperature can produce an energy process equivalent to the longer annealing at lower temperature. Here, the controlled growth rate depends on the heat transfer by convection in the liquid phase. The final crystalline morphology can be molded by the temperature gradient of the thermal process.

Rapid thermal annealing processes are successfully used in semiconductor industry and research. For instance to growth monocrystalline silicon material. For perovskite solar cells, rapid thermal annealing has already been used and proved as cost-effective solution to grow perovskites thin films of high optoelectronic quality and different compositions [35, 41–44].

The FIRA set-up

The FIRA oven is composed by an array of near-infrared halogen lamps. An hollow aluminum body provides a water-cooling system as shown in the cross section view in figure 2.23. Two gas inlets allows nitrogen or dry air to be pumped in during the FIRA processing. In a typical experiment, the perovskite solution is spin-coated onto an FTO or ITO substrate. These two transparent oxides are strong absorbers in the emission spectral range of the near-IR lamps. This allows a rapid heating of the substrate and, consequently, of the spin-coated perovskite layer. Indeed, the precursor solution film does not absorb the radiation, it exchange the heat with the underlying layer. During this process, rapid crystallization results in micrometer-sized crystal grains. The chamber temperature, the pulse intensity, and the pulse duration can be adjusted to control the crystal growth and nucleation. Once nucleation has occurred, it is followed by the growth of a crystalline phase. The intense FIRA flash leads to the rapid evaporation of the solvent and provides the driving force for the crystal nucleation and growth during which several intermediate metastable phases follow one another. A simplified view of these steps is visible in figure 2.24. If sufficiently low, diffusion kinetically limits the growth. In conclusion, the temperature, the speed of the heating, and the heating time control how supersaturation is reached [34].

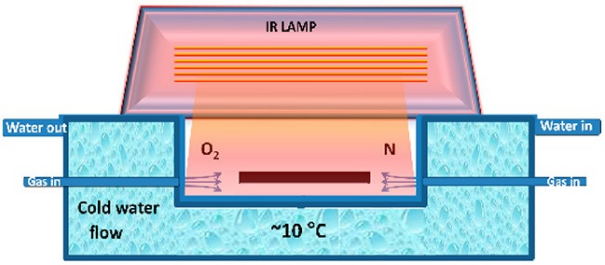

Figure 2.23. A cross-section view of the FIRA oven. The sample is placed into the sink and is exposed from the top by an array if IR Halogen lamps. The system is cooled down by a constant flow of water around the sink. To keep the sample under inert air during the irradiation, nitrogen or oxygen can be injected from the two inlets surrounding the sink. A pyrometer and a termocouple measure the temperature evolution in the sink and on the top of the substrates. Image source [42]

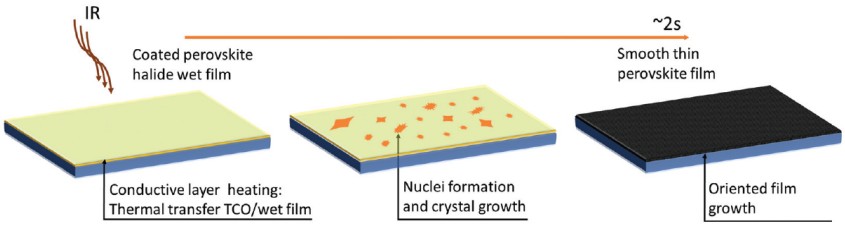

Figure 2.24. The sequential steps of the thin film perovskite formation. Image source [45].

Crystalline properties and growth dynamic in FIRA annealed perovskite films

In antisolvent method an high nucleation density is obtained by the reduction in solubility of the perovskite precursors followed by crystal growth. FIRA achieves the same effect by irradiating a lot of energy in short time. Due to this high heat input, FIRA lead to the growth of larger grains. Therefore, with this method, perovskite film crystallization can be completed in less then one second followed by thermal treatment to help the evaporation of the excess solvent [34].
Figure 2.25a shows a concentration profile (LaMer curve) during the different growth phases. C_s is the solubility limit of the solution, while C_c is a critical concentration value above which *self-seeding* is induced and it leads to crystallization from the solution. C_m is the maximal supersaturation above which the substance precipitates in an uncontrolled instantaneous self-nucleation. Up to t_1 the solution concentration increases due to the solvent evaporation. Then, between t_1 and t_2, the crystal nuclei forms by self-seeding. The subsequent crystal growth from the nuclei and further solvent removal due to evaporation results in a steady state concentration between C_s and C_c in the time interval t_2 to t_3. In antisolvent method, the supersaturation is reached by varying C_s, C_c, and C_m by adding a poor solvent for the perovskite. Here, the abrupt reduction of solubility is the cause for the high nucleation density. Indeed, by varying the degree of supersaturation, the spacing between nuclei can be tuned. In FIRA, the concentration in the perovskite solution is varied through solvent evaporation by thermal heating. The perovskite nucleation rate during FIRA annealing is

lower compared to the antisolvent method. This is due to either a lower supersaturation or a time-limitation of the nucleation phase by the shortness of the heating pulse. The lower nucleation density allows larger crystal domains beneficial for the solar cell's performances. In figure 2.25b is shown the surface temperature of the perovskite film, FTO and the temperature of the interal FIRA chamber as a function of time during and after a 2 seconds IR flash. The temperature on the top of perovskite reaches a peak of 70°C, that is far from the degradation temperature of perovskite above 100°C. Nevertheless, the FTO reaches a temperature of 480°C due to its strong absorbance in the IR range [35].

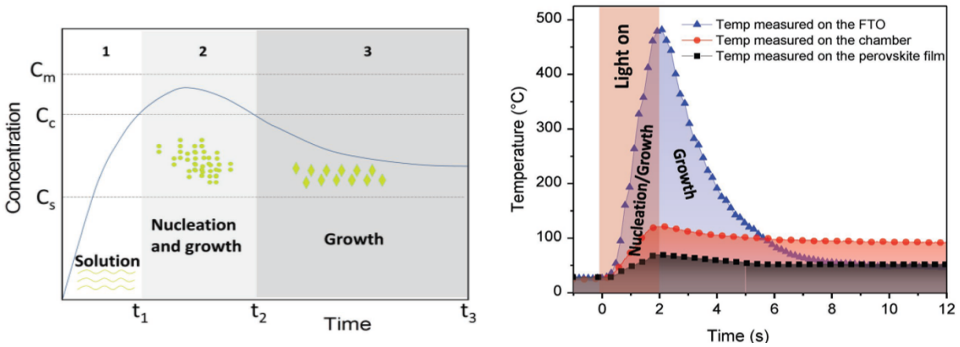

(a) **(b)**

Figure 2.25. **(a)** Schematic representation of the concentration variation during crystal nucleation and growth according to the LaMer curve. **(b)** Temperature evolution during the FIRA processing.

In this thesis work, perovskite layers were grown on top of a mesoporous titanium dioxide (TiO_2) layer. It worth to be mentioned that different mechanism of the crystal nucleation and growth are found in the presence of a mesoporous TiO_2 layer compared with the compact TiO_2 electrode. Indeed, each of these TiO_2 layers provides a different interfacial energy. Because of its porosity, the mesostructured TiO_2 has a higher effective interfacial energy than the planar TiO_2 electrode leading to larger grains for the planar case, and smaller for the mesoscopic layer as substrates [46].

Experimental methods and characterizations

3.1 Thin film processes for solar cell's fabrication

All the thin films that compose the solar cell's stack were formed on patterned FTO on glass substrates. In figure 3.1 are shown the specifications of the substrates. During the successive deposition steps, on each FTO square is realised a *pixel* where a pixel represents a cell. Therefore, each substrate hosts a total of two solar cells. To avoid any cross-talk between the two pixels, a line of FTO was removed by the supplying company.

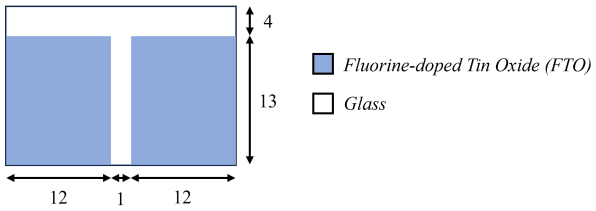

Figure 3.1. Patterned FTO on glass substrates purchased from ShangYang Solar Technology. The dimensions are expressed in millimeters.

3.1.1 Substrate preparation

In order to guarantee a proper interface between the deposited layers and the underlying FTO, all the substrates were washed with 2% of Hellmanex diluted in water, then acetone, and finally ethanol. The substrates with each of these solvents were kept for 10-15 minutes in an ultrasonic cleaner Branson 1510 and then, after the ethanol, they were dried with compressed air. Before proceeding with the deposition of the compact titanium dioxide (TiO_2) layer, the substrates were subjected to a 15 minutes treatment in a UVO (Ultra Violet Ozone) cleaner from Jelight Company, Inc. model 256 Series. The solar cells intended to target the best performances, were cleaned with a plasma cleaner Harrick-Plasma PDC-002-CE.

UV Ozone treatment

UV Ozone treatment allows the contamination removal from the surface of the samples, providing ultraclean surfaces. Using a high-power UV light source to generate ozone (O_3) and break down organic surface contaminants, the procedure can produce near-atomically clean surfaces without damaging the sample. Low-energy bonds such as the C-H bond are

replaced with higher energy groups such as C-OH. As a consequence, the surface energy of a substrate improves and this leads to an improved wettability too [47].

3.1.2 Spray pyrolysis for compact ETL deposition

Spray-pyrolysis is a thin film deposition method widely used in industry. This method generates an aerosol, that are solid or liquid droplets suspended in a carrier gas, in a nebuliser and are carried as a gas flow toward an hot plate where the substrate is located [48]. The compact TiO_2 layer was deposited by aerosol spray pyrolysis using oxygen as carrier gas. The precursor solution located in the nebuliser was composed by 0.4 ml of acetylacetone ($C_5H_8O_2$), 0.6 ml of Titanium diisopropoxide bis(acetylacetonate) stock solution (75% in Isopropanol), and 9 ml of ethanol. The substrates were placed on a hot plate and covered with a metal mask on the side opposite to the FTO etched edge. Then the hot plate was switched on and the substrates were heated up to 450°C for 12 min and then kept at this temperature for 15 min. After, the precursor solution was sprayed at a distance of about 20 cm with an inclination of 45°, with at least 20 s of delay between each spraying cycle. During each cycle, all the substrates on the hot plate had to be covered in few seconds. Once the solution was finished, the substrates were kept for 5 more minutes at 450°C and then the hotplate was switched off. The substrates were then removed from the hot surface once the temperature was below 150°C.

3.1.3 One-step spin-coating technique

Spin-coating technique is a method widely used at laboratory level to prepare thin films with homogeneous coatings. During sping-coating, the substrate is placed onto a rotating disk. To keep the substrate hold onto the disk during the successive rotation, vacuum is applied between the disk and the substrate. Then the liquid precursor is dropped in the middle of the substrate. This drop can happen either during the rotation (*dynamic deposition*), or before starting the rotation program (*static deposition*). During the spinning, the precursor solution is well dissipated and a thin film on the top of the substrate is formed. Thermal treatment may follow. The solar cell's fabrication steps that required spin coating are described below.

Mesoporous Titanium dioxide deposition

To deposit the mesoporous titanium dioxide layer for electron extraction, the one-step spin-coating technique was used. Before depositing the m-TiO_2, the substrates were subjected to a 15 minutes into the UVO cleaner. The precursor solution was prepared by mixing a 30 NR-D titania paste (Greatcell Solar) with ethanol in a weight ratio $m_{30NRD}/m_{ethanol} = 1/10$. This solution was then left stirring with a magnet for at least 12 hours before using it.
Before the spin coating, a piece of cellophane was placed to cover the sample at the edge where during the compact TiO_2 there was the mask. The static deposition followed by dropping 50 μl on the sample and spin coated with a speed of 4000 rpm, acceleration 2000 rpm, and for 10 s. Then the sample was dryed at 100°C on a hotplate for 10 min. Once all the samples were subjected to these steps, a multiple-steps sintering program followed with a duration of about 12 hours and a temperature ranging between 125 and 450°C.

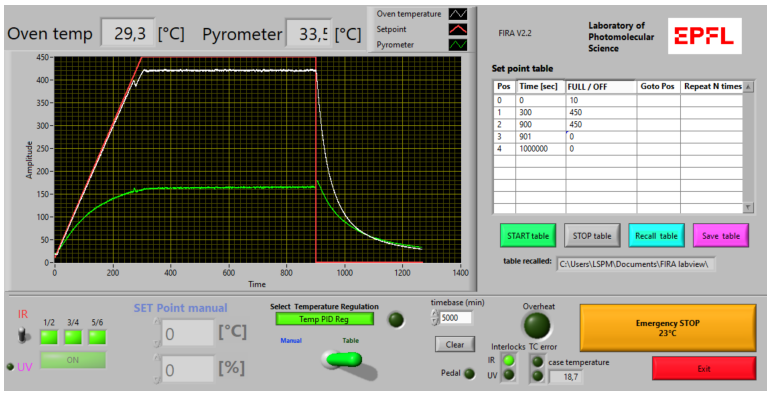

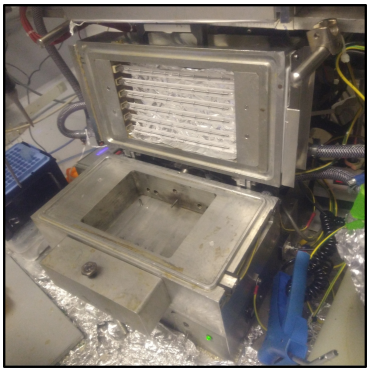

(a) **(b)**

Figure 3.2. **(a)** The FIRA control interface with all the commands and process parameters.**(b)** A picture of the FIRA oven used for the realization of all the film and devices of this project.

Perovskite deposition for FIRA method and passivation

The perovskite precursor was spread over the sample through spin-coating in a glovebox under inert atmosphere. 35 μl of solution was dropped statically on the sample and spinned with the following program: speed 4000 rpm, acceleration 1200 rpm, for 10 s. Then FIRA process followed as described in paragraph 3.1.4. The precursor perovskite solutions were prepared in a glovebox in nitrogen atmosphere with oxygen and H_2O levels below 7 ppm.

Spiro-OMeTAD and PTAA deposition

The deposition of the organic hole transport layers investigated in this work was performed after cooling the perovskite films and with the following spin-coating program: 50 μl, speed 3000 rpm, acceleration 1200 rpm, for 20 s. Spiro-OMeTAD (Sigma-Aldrich) was dissolved in chlorobenzene and p-doped with Li-TFSI (lithium bistrifluoromethanesulfonimidate) (Sigma-Aldrich) with the addition of 4-tert-butylpyridine (tBP) (Sigma-Aldrich) to improve the morphology. PTAA (poly(triaryl amine)) (Sigma-Aldrich) was dissolved in chlorobenzene without any dopant. The solutions were prepared in a glovebox in nitrogen atmosphere with oxygen and H_2O levels below 10 ppm.

3.1.4 FIRA processing

The FIRA oven was used for both thermal treatment of the samples, and, above all, for perovskite's thin film crystallization. In figure 3.2a is shown the LabView interface of the FIRA oven through which the system is controlled by the user. Different IR pulse can be set with different duration and the evolution of the heat into the sink and on the substrate is monitored through a termocouple and a pyrometer. The temperature variation is visible in the LabView plot together with the temperature setpoint. An annealing process on the samples coated with the ETL is performed into the FIRA oven before the perovskite growth. The annealing program is the one shown in figure 3.2a and the plot shows how the temperature

evolved in the oven up to few minutes after the end of the program. Then, the substrates were removed from the oven's sink and cooled down for few seconds. Then spin-coating of the perovskite followed with the method previously described in 3.1.3. The sample coated with the perovskite precursor was then placed in the FIRA oven and irradiated with a 640 ms pulse. Then, to allow excess solvent to evaporate, samples were placed on a hotplate for 2 hours. During these 2 hours a passivating agent named PEAI (Phenethylammonium iodide) (2 mg/ml dissolved in IPA (isopropyl alcohol)) was dynamically spin coated (60 μl, 3000 rpm, 1200 rpm acceleration, 20 s). At the end of these 2 hours, the samples were left cooling down for few minutes before the HTL deposition. All these steps were performed in a glovebox with monitored temperature and humidity levels.

3.1.5 Thermal evaporation

Molybdenum oxide films were deposited by thermal evaporation technique using a nanoPVD-T15A from Moorfield Nanotechnology. The Molybdenum(VI) oxide powder (Sigma-Aldrich) is evaporated from an aluminium oxide crucible by supplying a current of $\simeq 96$ A. This input guarantees a deposition rate of 0.02 Å/s. Gold films were deposited with a FTC-1800 Kurt J. Lesker with a variable deposition rate and a final thickness of 80 nm for all the samples. Thermal evaporation is a physical vapor deposition (PVD) technique where films growth is achieved by evaporating the material (in the shape of small grains or slugs) placed in a crucible or boat heated up by Joule effect. It works under low pressure (10^{-5} Pa) to increase the mean free path and guarantees a line-of-sight deposition.

3.1.6 RF and DC magnetron sputtering

Silver and Nickel oxide (NiO_x) films were deposited respectively by DC and RF magnetron sputtering. The sputtering facility was an Alliance-Concept DP 650 with a DC generator Huttinger TruPlasma 3002 and RF generator Huttinger PFG 600 RF. All the depositions were performed at room temperature (RT) with a pressure lower than 1×10^{-6} mbar. NiO_x had a deposition rate of 1.4 Å/s, while for the Ag, two deposition rates were available: 2.6 Å/s and 17.4 Å/s. The DC sputtering system is composed of a chamber under vacuum partially filled with a gas at low pressure (Argon for non-reactive sputtering). In the chamber there are two electrodes: the anode (the substrate) positively charged and the cathode (the target) negatively charged. By applying an potential difference between the two, the deposition process is initiated. Radio Frequency (RF) sputtering is used for insulating materials in which DC power cannot flow current through and cannot initiates a plasma. The RF frequency of 13.56 MHz is typically applied between the tow electrodes. With the magnetron sputtering, a magnetic field is applied perpendicular to the electric field leading the electrons to follow a gyrating motion. This increases the plasma density [49].

3.1.7 Solar cell's encapsulation

The solar cell's encapsulation was performed by depositing a 10 μm layer of parylene with a Comelec C-30-S. Parylene is a polymer deposited at room temperature under vacuum. It guarantees conformal layers and resistance to many solvents. It is deposited by heating the

dimmer at about 150°C. Than it diffuses to Pyrolysis chamber at 670°C and is diffused to the room temperature or slightly heated (80°C) process chamber, and condensates to fabricate Parylene layer [50].

3.2 Characterization methods

3.2.1 Solar simulator for JV measurements

The solar simulator is a device that exploits a light source to produce an energy current density per photon wavelength with the form and magnitude as the solar spectrum shown in 2.5b. The shape and intensity of the solar spectrum is due to the Sun's temperature of about 5800 K. Nevertheless, its simulation is possible because, even though the simulating light source cannot reach such temperature, the solid angle subtended by the radiation source can be increased to reach the same spectrum. The relationship between the temperature and the energy current density emitted by a nonblack body in the energy interval d$h\nu$ into the solid angle element dΩ is [16]:

$$dI_\lambda(h\nu) = \frac{a(h\nu)d\Omega}{4\pi^3\hbar^3(c_0/n)^2}\frac{(h\nu)^2}{exp(h\nu/k_BT)-1}dh\nu \tag{3.1}$$

The system employed during the measurements is composed by an arc lamp Class AAA sun simulator from Newport, a multimeter model 2401 from Keithley Instruments to perform the voltage ramp from 1.2 to 0 V (reverse scanning) with a step of 0.01 V. The sample is measured in the dark box visible in figure 3.3a and placed in contact with the sample holder in figure 3.3b. The pins of the holder will be in direct contact with the gold electrodes on the cell. During the measurement, the current density J_{sc} is calculated according to the formula I_{sc}/A, where A is equal to 0.158 cm^2. This is the exposed area and corresponds to the dimension of the slits of the sample holder mask visible in figure 3.3b.

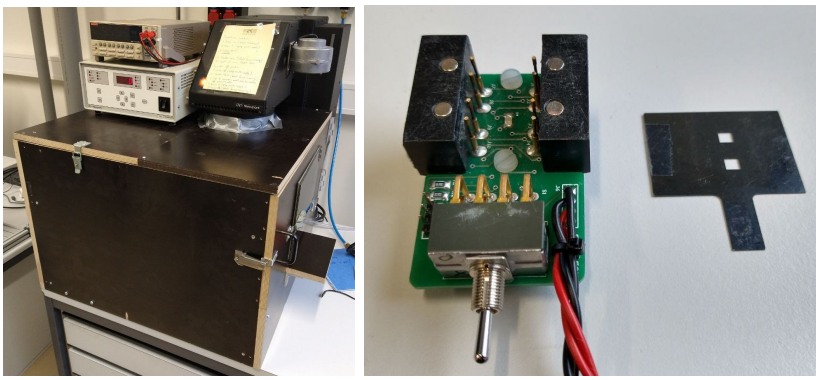

(a) **(b)**

Figure 3.3. **(a)** The solar simulator *Oriel* for JV measurements. **(b)** The sample holder where the solar cell is placed during the JV scanning and the mask used to expose the active area.

3.2.2 Incident photon to current conversion efficiency (IPCE)

The incident photon to current conversion efficiency (IPCE) of the cells was measured with a Ariadne system from Cicci Research. An Argon lamp is employed as excitation source and a monocromator selects the wavelength to excite the sample. The solar cell is connected to an external circuit (through the mask holder shown in 3.3b) to read the charge collection efficiency. The measurements were performed in the wavelength range 300-900 nm.

3.2.3 UV-Vis photospectrometry

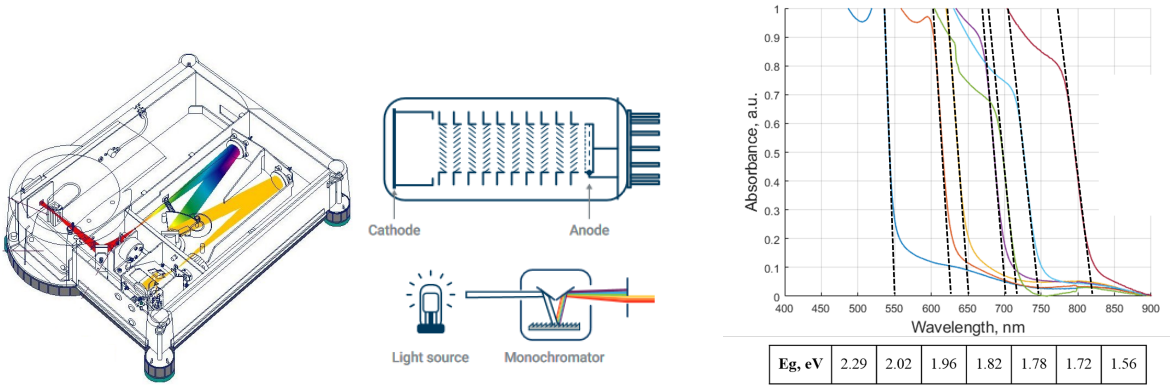

Eg, eV	2.29	2.02	1.96	1.82	1.78	1.72	1.56

(a) **(b)** **(c)**

Figure 3.4. **(a)** The inner configuration of a Cary 50 photospectrometer (from Varian Cary user manual). A Cary 5 inner view was not available. **(b)** Photomultiplier tube (top) and monochromator (bottom) simplified schemes (Agilent Technologies [51]). **(c)** An example of the derivation method of the bandgap given the absorbance spectra.

For UV-Vis photospectrometry analysis, a Varian Cary 5 UV/VIS/NIR spectrophotometer was used. In figure 3.4a is shown the inner configuration of a Cary 50 model whose design is similar to the Cary 5 model. The device exploits a Xenon flash lamp that emits short light pulses during the measurement. Since all the light sources emit a broad spectrum, to narrow the light down to a selected wavelength band, the light passes through a monochromator. This component consists of an entrance slit, a dispersion device (e.g. a grating) that spread the light into different wavelengths and allow the selection of the chosen wavelength range, and an exit slit. During the measurement, the selected wavelength that exits the slit gradually changes, the sample is exposed to this source, and the output light (absorbed and/or reflected) is captured by a detector. The Cary 5 has installed a photomultiplier tube whose simplified scheme is shown in figure 3.4b. Such detector combines signal conversion (optical/electrical) and amplification within the body of the tube. It guarantees a good sensitivity over the entire UV-visible range from 200 to 900 nm.
The final data is reported in a.u. for the absorbance measurement mode and in % for the transmittance measurement mode. For the estimation of the bandgap from the absorbance plot, a straight line tangent to the main rise of the curve was plotted. Its intersection with the x-axis was the value of wavelength from which the bandgap was evaluated. In figure

3.4c are shown some examples. The measurements were performed in the wavelength range 350-900 nm.

Average Visible Transmittance calculation

The Average Visible Transmittance (AVT) was calculated as the integration of the UV-Vis transmission spectrum ($T(\lambda)$) and AM1.5 photon flux ($j_{E,AM1.5}(\lambda)$) weighted with respect to the photoptic response of the human eye ($V(\lambda)$) in the range 350-800 nm:

$$AVT = \frac{\int_{350nm}^{800nm} T(\lambda)V(\lambda)j_{E,AM1.5}(\lambda)\,d\lambda}{\int_{350nm}^{800nm} V(\lambda)j_{E,AM1.5}(\lambda)\,d\lambda} \tag{3.2}$$

The computation of the AVTs was possible thanks to the spreadsheet provided by C. Yang et al. (2019) [52].

3.2.4 Photoluminescence spectroscopy

Steady-state photoluminescence measurements were performed with a Fluorolog3-222 from Jobin Yvon Horiba. The system generates a beam of light that is filtered by an excitation spectrometer and allows a single wavelength of light to reach the sample. Once the sample is excited by the single-wavelength radiation, it reemit a signal whose spectral content is converged toward another emission spectrometer and sent to a photomultiplier detector. By stepping either or both spectrometers through a wavelength region, and recording the variation in intensity as a function of wavelength, a spectrum is produced [53].

3.2.5 Optical Transmission Microscopy

Optical Transmission Microscopy (OTM) was employed to analyze the perovskite thin films. A LED illuminates the sample from the bottom and the transmitted light is converged toward the lens of the optical microscope from Olympus (magnification 10X). Then, the collected light is captured by a CS505 camera from Thorlabs.

3.2.6 Scanning Electron Microscopy

The scanning electron microscopy (SEM) images were recorded using a Zeiss Gemini-300 (FEG, Gemini 1 column) microscope with an acceleration voltage of 3.00 kV. The SEM technique exploits an electron beam focused in to a small probe and scanned in a raster pattern across the surface of a sample. The most commonly detected signals are secondary electrons and backscattered electrons. By collecting the charges, and correlating signal intensity with probe position, images of the sample surface are generated.

3.2.7 Surface roughness characterization

The morphological surface analyses of the deposited thin films were performed with a DeltakXT Bruker as the one shown in figure 3.5a. This system exploits a stylus physically in contact with the surface being measured and a transducer to convert its vertical movement into an electrical signal. A scheme of the typical configuration of a mechanical stylus instrument

is visible in figure 3.5b where both mechanical control systems and electronic amplifiers for signal boosting are available. The part of the stylus in contact with the surface is usually a diamond tip with a carefully manufactured profile. For the measurements, a stylus with a radius of 0.7 μm was exploited. The force of the stylus can be tuned from 1 mg to 15 mg according to the fragility of the surface and the precision needed. If the force is too high, damage may occur to the surface being measured. If the force is too low, the stylus will not stay reliably in contact with the surface [54]. For the measurement of the organic perovskite layers, a force of 10 mg was applied. To measure the mathematical parameters a *map scan* was performed witha scan area of 1 mm^2. A vertical resolution of 0.333 $\mu m/point$ was employed.

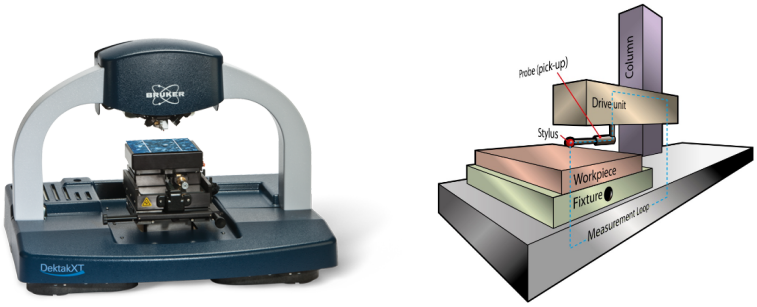

(a) **(b)**

Figure 3.5. **(a)** The DeltakXT profilometer by Bruker. Image from the Bruker website. **(b)** A scheme with all the elements of the typical stylus instrument (standard ISO 3274) [54].

3.2.8 Light soaking stability measurements

These stability measurements were performed with a Fluxium system composed by a Litos Lite for JV measurements and lamps provided by Wavelabs. The samples were illuminated with a constant AM1.5 spectrum (1000 W/m^2), average temperature of 22°C, and relative humidity 0%. The sampling rate for the photocurrent and voltage was 1 pt/min.

3.2.9 Four-Probe method for sheet resistance measurement

To measure the sheet resistance of thin films, the four-probe method was employed. This method contacts the sample with four pins to reduce the contact resistances that, otherwise, would affect the measurement. The 4-probe was automatically controlled by a LabVIEW software that drives a multimeter from Keithley Instruments model 2401 to accomplish the measurement. The software executes a current ramping from -0.05 to 0.05 A with a step of 0.01 A.

Results and discussion

To achieve high performances perovskite solar cells, the developed final wide bandgap device was optimized from both the perovskite composition and the hole extraction layer by playing with different charge selective materials. Finally, by looking to a multi-junction scenario, the gold electrode contact employed at the lab-scale level to characterize the solar devices was substituted by a thinner transparent electrode. It allows the light not absorbed by the wide bandgap perovskite layer, to reach the bottom solar cell.

Working principle of the realized solar cells

In figure 4.1a is shown the top view and equivalent circuit of the *n-i-p* solar devices realized during the project. Each device is composed by two separated cells (or pixels). The yellow square in the middle is the gold electrode acting as ohmic contact and with interfacing the hole transport layer (HTL). In figure 4.1b, it is the electrode on top of the cell. While, the gold electrodes on the bottom are connected to the FTO layer with interface with the electron transport layer (ETL).

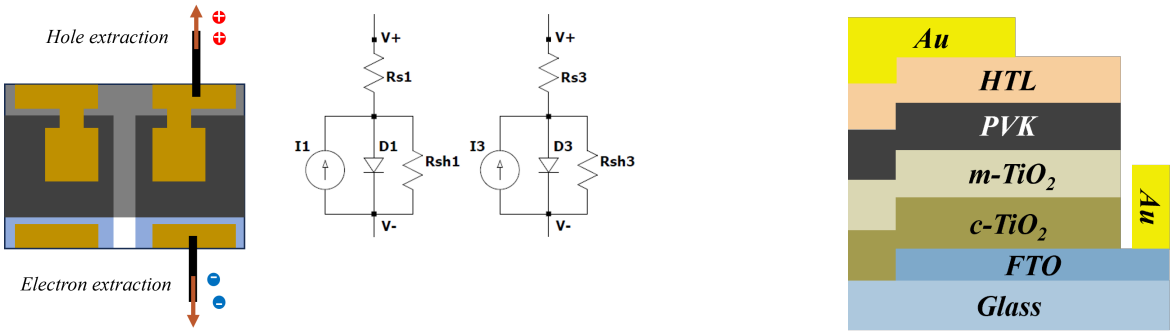

(a) **(b)**

Figure 4.1. **(a)** The top view and equivalent circuit of the solar devices realized during this thesis work. Each device is composed by two cells (or pixels). **(b)** Schematic of the device structure.

4.1 Wide bandgap perovskite solar cell optimization

Previous studies showed that FIRA processing lead to good quality and highly stable $MAPbI_3$ [35, 43] and $FAPbI_3$ [44] perovskites films. Specifically, Formamidinium (FA) was proved to be a more stable cation compared to the volatile Methylammonium (MA) [55]. Since device stability under standard atmospheric conditions are one of the main issues in perovskite solar cell technology [56], Formamidinium has been considered as a reference for developing wide bandgap absorbers for tandem solar cell applications. In figure 4.2 are shown the SEM and optical images of one of the $FAPbI_3$ solar cell realized with FIRA during this project. As expected, the perovskite films look compact and with few defects by the electron beam intensity. The grain domains show a spherulite structure with a highly branched polycrystalline crystallization pattern. The center of the grain (darker in the optical images) is the nucleation site from which the growth develop radially with a intermittently branching to maintain a space filling character (category 1 spherulites). This spherulite growth is due to orientational defects that arise from defects and heterogeneities as phase separations [57]. From the SEM image, some intra-grain defects are visible. These can lead to contacts between the blocking layers with a consequent reduction of the performances.

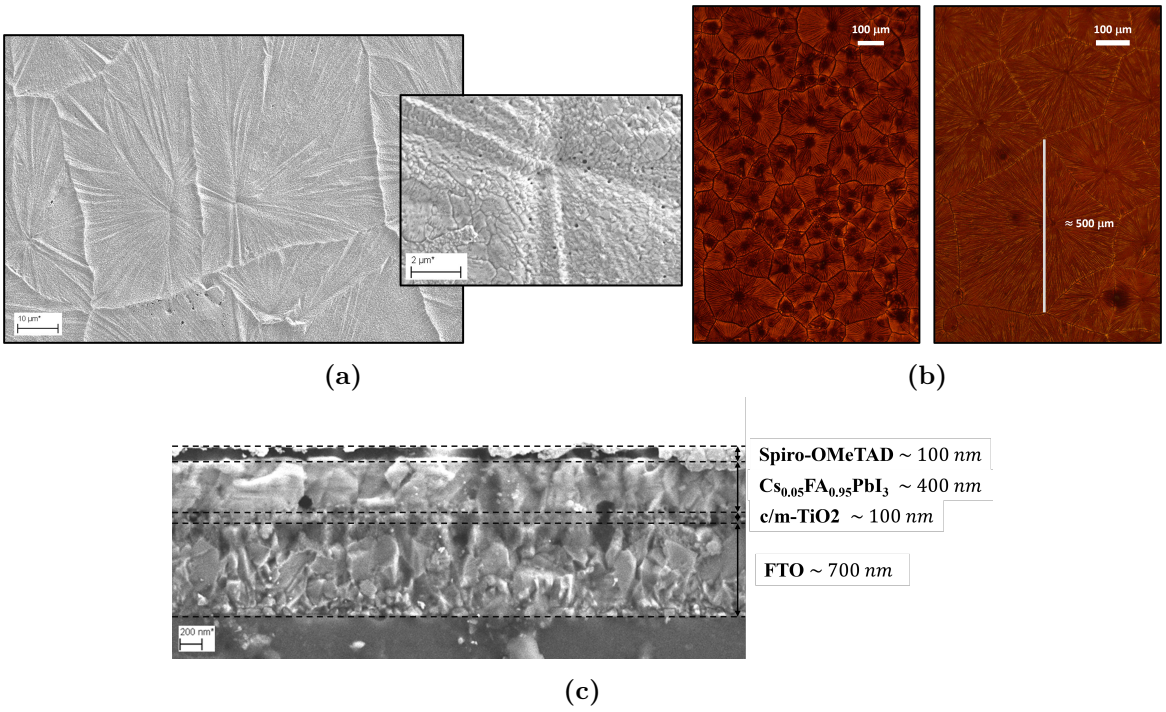

Figure 4.2. **(a)** A SEM top-view image of a $Cs_{0.05}FA_{0.95}PbI_3$ perovskite film. Some defects are present in the film (encircled in red). The left picture has a scale of 10 μm, the right 2 μm **(b)** Optical transmission images of two different $Cs_{0.05}FA_{0.95}PbI_3$ films. Scale 100 μm. Between different samples, the grain dimension can vary from tens of micrometers up to about 500 μm as highlighted in the second picture. **(c)** Cross-section SEM image of a full solar cell device. Scale 200 nm.

In a prospect of a stable device, all the control perovskite solar cells were realized with 5% of

Cesium in replacement of FA as cation to reduce phase segregation phenomena [58]. Therefore, the stoichiometry of the control devices was $Cs_{0.05}FA_{0.95}PbI_3$. This film composition provides a bandgap of about 1.55 eV and it was chosen as bottom sub-cell for a perovskite-on-perovskite tandem solar cell. From both the SEM and optical images, no substantial differences are noticed with respect to the pure FA composition. According to theoretical studies on perovskite tandem solar cells [33, 59], for a bottom sub-cell with a bandgap equal to 1.55 eV as it is for perovskite phase $FAPbI_3$, the top sub-cell should have a bandgap of around 1.9-2.1 eV. To widen the bandgap starting from the $Cs_{0.05}FA_{0.95}PbI_3$ composition, the Bromine (Br) and Chlorine (Cl) anion fraction was increased with a consequent reduction of the Iodine (I) one.

Bromine anion mixture

In figure 4.3a is shown the variation of the absorbance spectra performed by UV-Vis photospectrometry while increasing the bromine (Br^-) fraction. The rise of the absorbance spectrum is shifting toward smaller wavelengths (larger energies) thus higher energetic photons are absorbed, while the low energetic ones will be transmitted and not detected. The bandgaps estimated from the absorbance plot show a linear trend with the increase of the Br fraction as visible in 4.3b. This linear behavior is coherent with previous wide bandgap bromine studies [41, 55]. The composition $Cs_{0.05}FA_{0.95}Pb(I_{0.3}Br_{0.7})_3$ is the one that leads to a bandgap equal to about 2-1.9 eV that is the target for the final perovskite-on-perovskite solar cell. In 4.4a are shown the optical images of some of the analyzed high-bromine con-

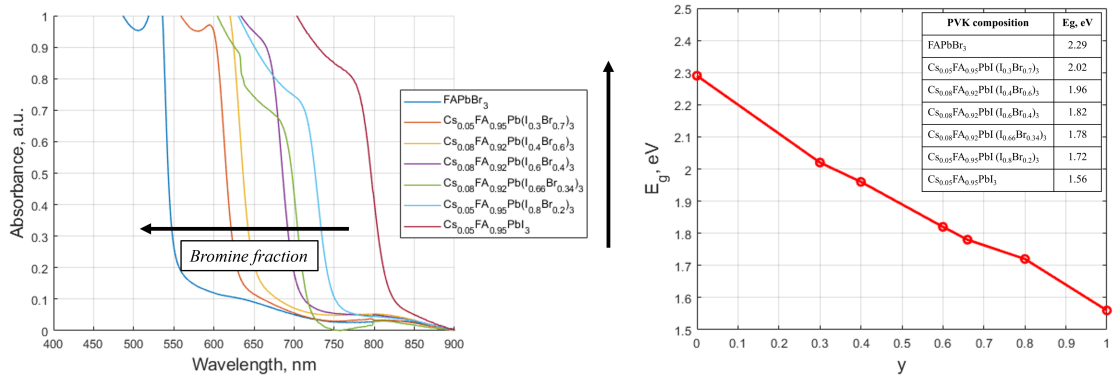

(a) **(b)**

Figure 4.3. **(a)** Absorbance spectra for different bromide compositions. The black arrows point toward the direction of the increasing fraction of bromine for the plots and the legend. **(b)** The estimated bandgaps for different values of y considering an anion composition of $(I_yBr_{1-y})_3$.

tent perovskite layers. It is possible to notice that the $FAPbBr_3$ film looks very rough with amorphous characteristics within the grains. The quality of the films tend to increase while moving toward higher iodine content films. Indeed, for the $Cs_{0.08}FA_{0.92}Pb(I_{0.66}Br_{0.34})_3$ the compactness, homogeneity, and dimension of the various grains is closer to the control sample of figure 4.2b. But, to accomplish the bandgap requirement, Br^- must be included. In 4.4a

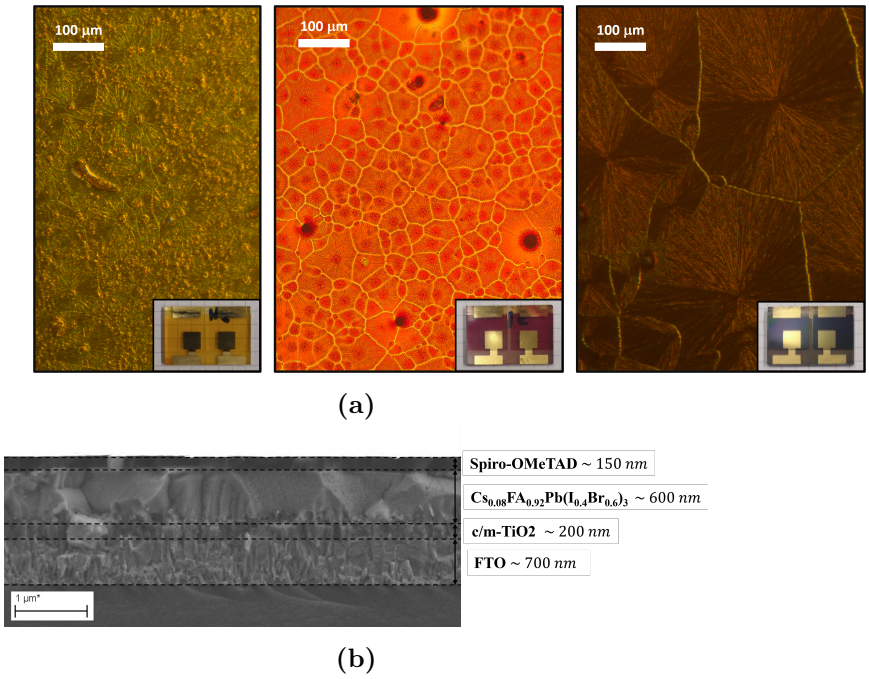

Figure 4.4. **(a)** From left to the right the optical images of a $FAPbBr_3$, $Cs_{0.05}FA_{0.95}Pb(I_{0.3}Br_{0.7})_3$, and $Cs_{0.08}FA_{0.92}Pb(I_{0.66}Br_{0.34})_3$. The corresponding fabricated devices for each condition are shown. It is possible to see how the color of the sample evolves with the bandgap. **(b)** A SEM cross-section view of one of the rich bromine conditions.

the $Cs_{0.05}FA_{0.95}Pb(I_{0.3}Br_{0.7})_3$ film is also depicted. In order to obtain better films the cation composition was varied by substituting MA and Cs to FA in small fractions without affecting the bandgap [60]. To assess the performances of the various perovskite compositions, several solar cell devices were fabricated and measured. In figure 4.5 are shown the boxplot data of the short circuit current (J_{sc}), open circuit voltage (V_{oc}), fill factor (FF), and power conversion efficiency (PCE) for different cation compositions of $Cs_xMA_yFA_{1-x-y}(I_{0.3}Br_{0.7})_3$ resulting from the JV analyses under solar simulator. The best performing conditions overall seem to be the $Cs_{0.05}FA_{0.95}Pb(I_{0.3}Br_{0.7})_3$ and the $Cs_{0.05}MA_{0.15}FA_{0.80}Pb(I_{0.3}Br_{0.7})_3$. In literature, these cation compositions lead to some of the record efficiencies for bandgaps between 1.6 and 1.8 eV. For bandgaps around 2 eV the best performances are observed for perovskites with cesium compositions around the 15% [61,62]. On the contrary, by using FIRA with the pulse of 640 ms, cesium seems not improving the performances. This is visible in the results in figure 4.5. Methylammonium incorporation in $FAPbI_3$ was already explored with successful results [25, 63]. By adding 15% of MA^+ cations the cubic phase was stabilized at room temperature. Moreover higher quality perovskite layers were observed. But, on the other hand MA inclusion lead to an increase of degradation by contact with humidity [55,64].

Electrical performances such as the J_{sc} of the wide bandgap devices cannot be compared directly with the J_{sc} of narrow bandgap control samples since, as expected, wider is the bandgap and lower will certainly be the generated photocurrent. Therefore, to allow a "fair" comparison, the Incident Photon to Current Conversion Efficiency (IPCE) analysis

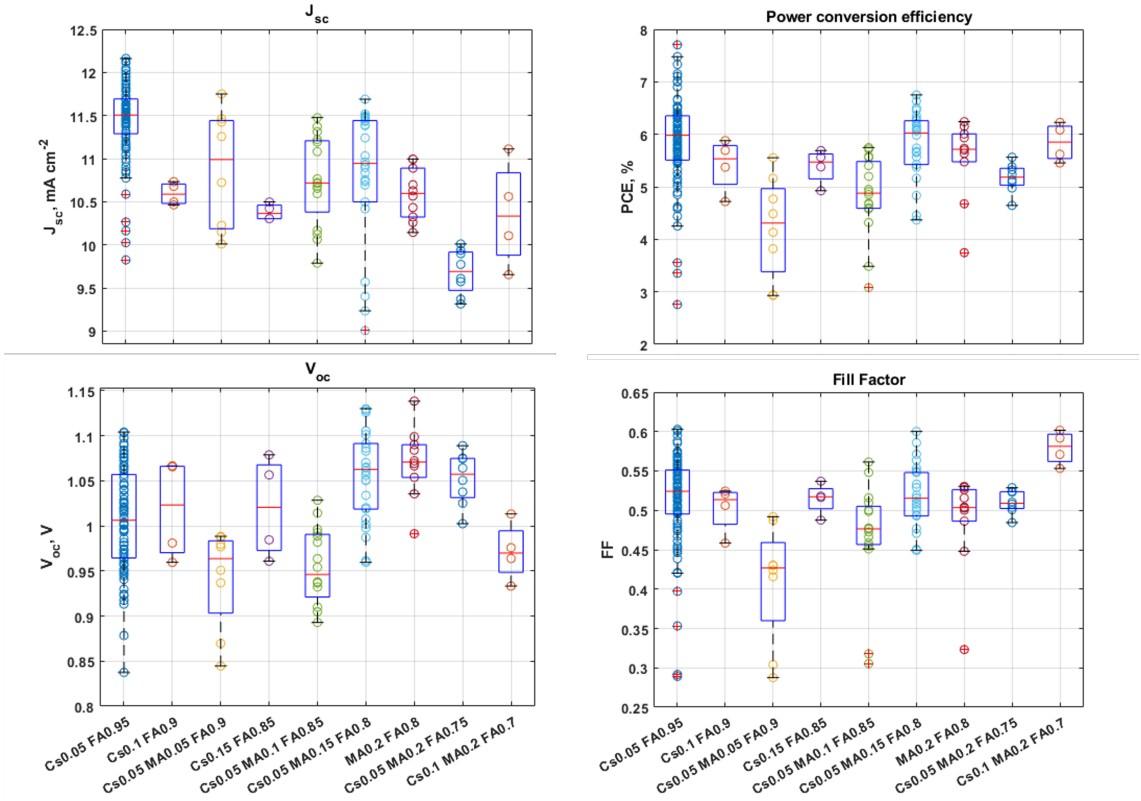

Figure 4.5. From the top left anticlockwise the short circuit current, open circuit voltage, fill factor, and power conversion efficiency for different cation compositions and fixed anion stoichiometry at $(I_{0.3}Br_{0.7})_3$.

was employed. This parameter evaluates how effectively the electron-hole pairs (excitons) are collected in the device by the number of incident photons at each wavelength. Indeed, by looking at the IPCE results in figure 4.6a, the control and wide bandgap samples can be compared in the wavelength range where both absorb the electromagnetic spectrum. The $Cs_{0.05}FA_{0.95}Pb(I_{0.3}Br_{0.7})_3$ condition is the one that shows an IPCE closer to the control. The efficiency decreases for the other compositions, even for the other wide bandgap good candidate, the $Cs_{0.05}MA_{0.15}FA_{0.80}Pb(I_{0.3}Br_{0.7})_3$ that showed good performances in terms of V_{oc} and PCE. The same trend can be noticed by looking at the current density plot in figure 4.6b. By looking at these exrternal quantum efficiency (EQE) spectra, the bandgap of the films can be derived. Indeed, the drop of efficiency tells us the wavelength after which the material does not absorb the electromagnetic radiation. To further investigate these different results, morphological surface analyses were performed. The profilometer results show an average roughness comparable between the control sample (67 nm) and the $Cs_{0.05}FA_{0.95}Pb(I_{0.3}Br_{0.7})_3$ (74 nm). Moreover, the grains show in both cases a spherulite structure. From the optical images the $Cs_{0.05}FA_{0.95}Pb(I_{0.3}Br_{0.7})_3$ film looks homogeneous within the grain and comparable with the control optical image. Different behavior can be observed for the $Cs_{0.05}MA_{0.15}FA_{0.80}Pb(I_{0.3}Br_{0.7})_3$ film, where each grain show intragrain uneven coverage. Indeed, brighter spots and lines are visible in the optical picture. The average

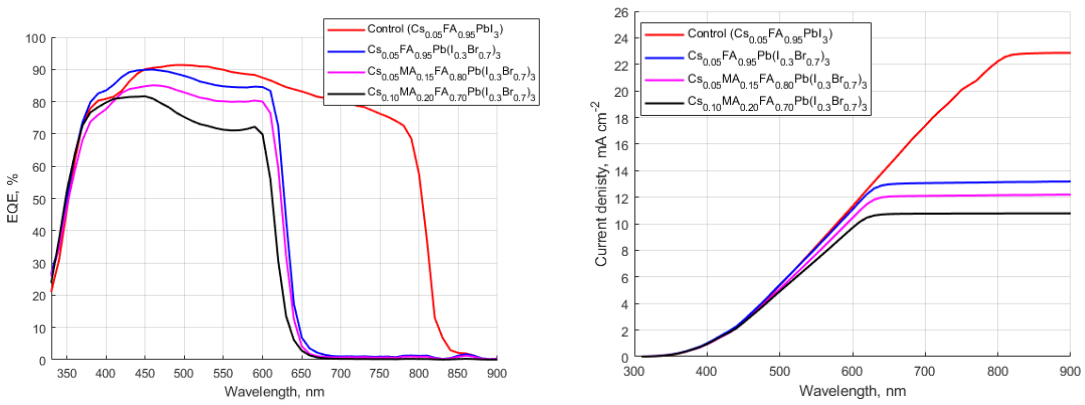

(a) **(b)**

Figure 4.6. **(a)** IPCE (EQE) plot for different bromine conditions. **(b)** The current obtained by integrating the EQE plot. The plateau of the current corresponds to the short circuit current.

roughness is higher with respect to the other two explored cases. All these observations and results lead to the choice of $Cs_{0.05}FA_{0.95}Pb(I_{0.3}Br_{0.7})_3$ as the best rich bromine wide bandgap perovskite composition.

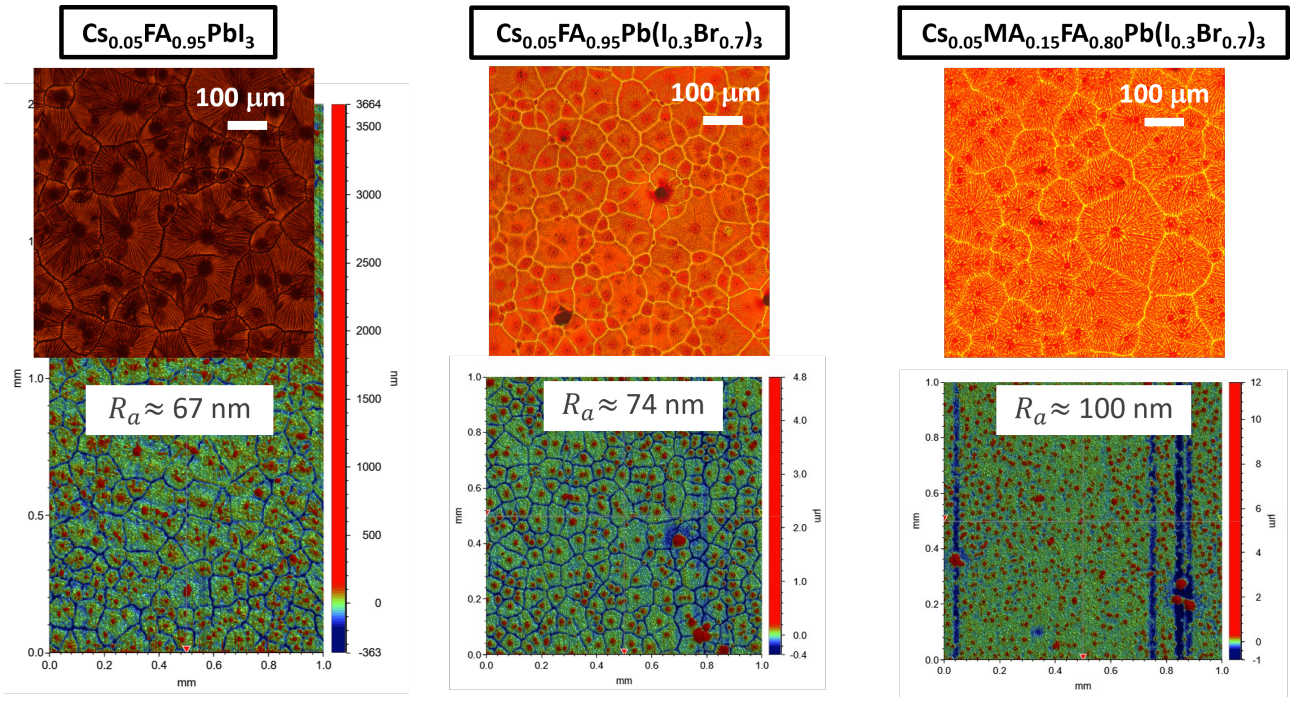

Figure 4.7. Profilometry and optical images for different perovskite films. Here, the best performing wide bandgap perovskite compositions are shown together with the control. The average roughness R_a is indicated in the pictures. Each R_a was derived by doing the average of the evaluated arithmetic mean deviation from the center line of different measurements.

Chlorine mix anion

Another option considered during the work was to use another halogen atom: the chlorine (Cl). Cl^- as anion mixed widens the bandgap when substituted to I^- as anion [25,61,62,65]. As already seen for Br^-, the rise in UV-Vis spectra blueshifts with the addition of Cl^- fraction. This is visible in figure 4.8a. But, contrarily to the previously seen high Br^- content films, now the absorbance spectra present several excitonic peaks. In a semiconductor devoted to photovoltaic applications, the charge separation is essential to deliver efficiently the carriers to the selective electrodes. The presence of excitonic peaks in chlorine rich perovskites absorbance spectra imply the presence of many generated electron-hole pairs bounded by Coulombic interaction with short lifetime [60]. To further investigate the quality

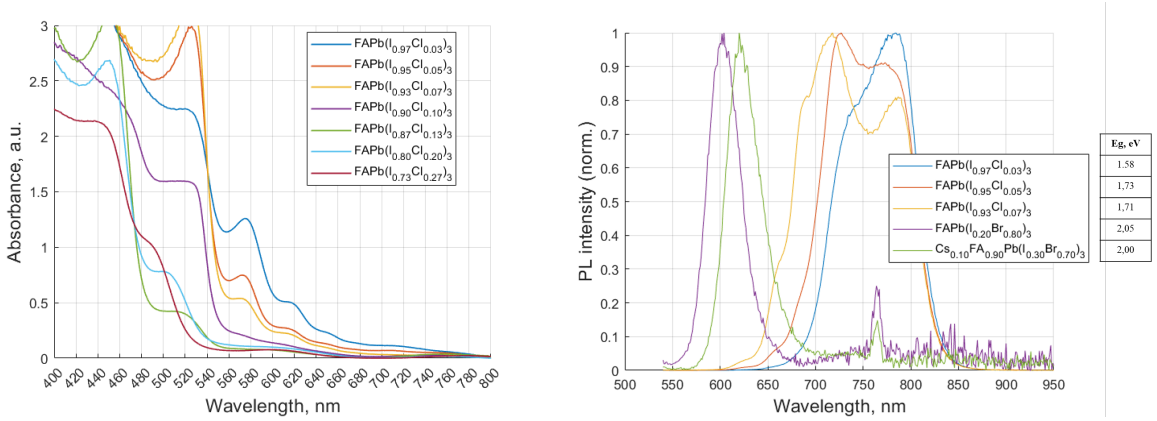

(a) **(b)**

Figure 4.8. **(a)** Absorbance spectra for different $FAPb(I_xCl_{1-x})_3$ compositions with an increasing chlorine fraction from the right to the left. **(b)** Normalized PL spectra for some chloride compositions compared with two bromine examples. The corresponding estimated bandgaps from the PL spectra are listed near the legend for each condition.

of the chlorine layers and their optoelectronic response, steady-state photoluminescence (PL) analyses were performed on some perovskite films. In figure 4.8b are depicted the normalized PL signals of different chlorine and bromine compositions. Normalization was necessary since the perovskite films were deposited on the TiO_2 ETL to guarantee the same interfacial energy for perovskite growth. This caused the quenching of some PL signals. The rich bromine conditions show a sharp peak around 600 nm that corresponds to an energy of about 2 eV. This value is in accordance with the bandgap value deduced from the absorbance spectra of figure 4.3a. Therefore, rich bromine films as the $Cs_{0.10}FA_{0.90}Pb(I_{0.3}Br_{0.7})_3$ have their main radiative recombination peak at the energy value corresponding to the optical bandgap of the material. Different behavior is observed in Cl-contain perovskite films. Here, the PL peaks are broader and far from the absorbance peaks visible in the UV-Vis plots of 4.8a. Figure 4.9a highlight this trend by comparing the UV-Vis and PL spectra for the control, 70 % bromine, and 3 % chlorine films. While the rich bromine and control film have their PL peak at the same wavelength of the absorbance rise, the 3 % chlorine film has the broad PL peak around 750 nm. At this wavelength, also the $Cs_{0.10}FA_{0.90}Pb(I_{0.3}Br_{0.7})_3$ film show a small

peak. According to the studies conducted by O. Shargaieva et al. [66] these signals at 750 nm are consequence of $[PbI_3]^{1-}$ and $[PbI_4]^{2-}$ polyiodide plumbate complexes that exhibit large Stokes shift compared to the absorption band. The presence of such complexes might cause defect states which reduce the optoelectronic properties of the perovskite semiconductor [67]. Therefore, different material compositions can be found in the exposed area during the PL measurements. The higher intensity of the 750 nm signal in the chlorine-containing films compared to the rich bromine one can be one explanation of the lower quality of the chlorine films. By looking at figure 4.9b the same behavior is visible by increasing the chlorine percentage. To obtain the target bandgap of 2 eV, rise of the absorbance plot should be at about 620 nm. A small amount of chlorine seems causing a large bandgap blueshift that this target value is missed.

To verify the performances of the solar cells realized with chlorine-containing films, some

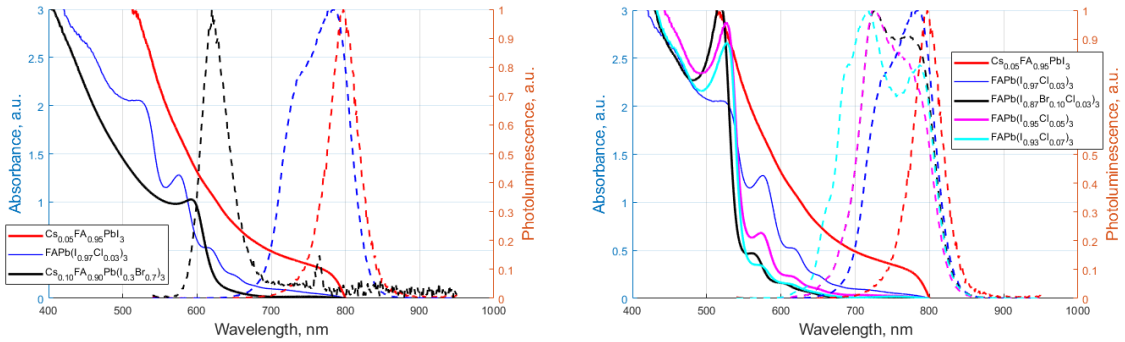

(a) **(b)**

Figure 4.9. The absorbance (left y-axis) and PL signals (right y-axis) for different perovskite films. **(a)** Here three conditions are compared: the control, rich bromine, and 3% chlorine films. **(b)** Different chlorine compositions are compared.

devices were realized and their EQE evaluated. In figure 4.11 are compared the EQE spectra for two chlorine composition with the best 2-1.9 eV rich-bromine film. The devices with chlorine show a poor EQE in the absorbing range of wavelenghts, and well below the 85% value reached by the other conditions. Before concluding the part dedicated to the anion and cation alloying, the last comments are dedicated to the structural properties of the realized films. A top view SEM images shown in figure 4.11. The uniform spherulitic growth during the FIRA processing of the control samples lead to compact grains as highlighted in the picture. Similar trend is visible for the $Cs_{0.05}FA_{0.95}Pb(I_{0.3}Br_{0.7})_3$ film. Here, a continuous pinhole-free film with full surface coverage was obtained. On the other hand, different results were obtained for the chlorine-composed sample. At macroscopic scale, the crystals look formed with a well defined nucleation center. But, by magnifying the crystallites, particles aggregations are visible on the surface. This phenomenon was observed for all the other chlorine based samples where the amount of these imperfections was increasing with the chlorine content. Such non-uniform growth can be one reason behind the inadequate performances of the chlorine alloying in $FAPbI_3$.

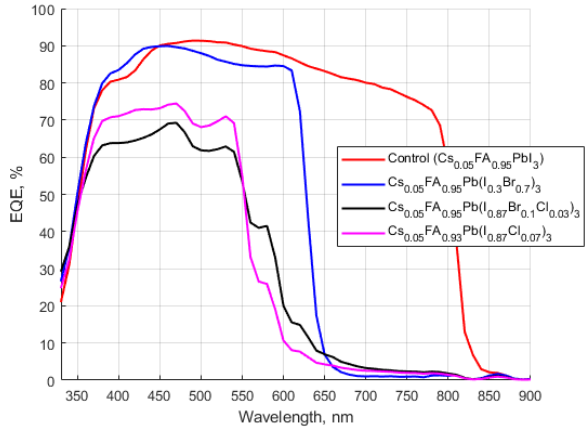

Figure 4.10. IPCE results for two chlorine conditions compared with the best rich bromine condition and the control $Cs_{0.05}FA_{0.95}PbI_3$.

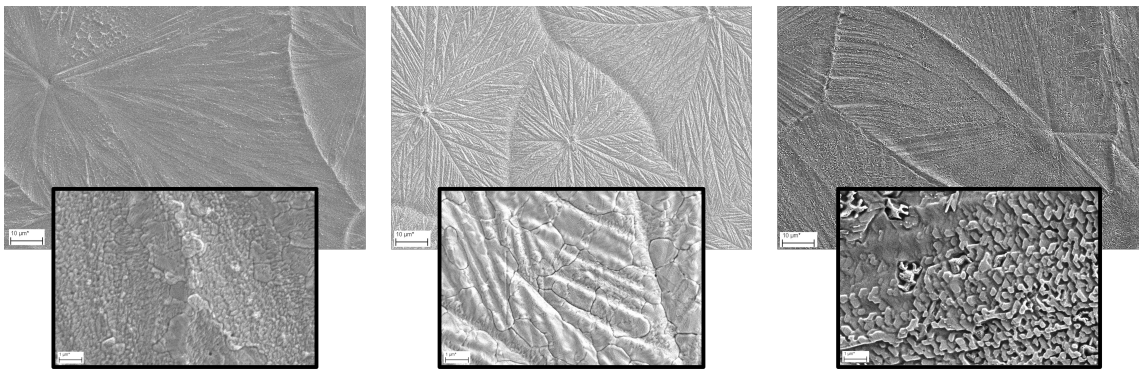

Figure 4.11. SEM images for different perovskite compositions. From the left to the right: $Cs_{0.05}FA_{0.95}PbI_3$ (control), $Cs_{0.05}FA_{0.95}Pb(I_{0.3}Br_{0.7})_3$, and $FAPb(I_{0.8}Cl_{0.2})_3$. Each image was magnified in the grain. The scales are 10 μm and 1 μm.

Further optimizations

To obtain better performances from the realized devices, some attempts of perovskite thickness optimization were performed. To allow an efficient charge extraction in solar cells, the diffusion length of the photogenerated carriers must be longer than the distance to the selective electrode for that charge [16]. According to this rule, thinner is the active layer, higher is the probability extract the carriers from the cell and sent to the load. On the other hand, a too thin material lead to a reduction of the absorption probability of the impinging photons. A trade-off between these two requirements is needed. Most of the devices realized during this work were prepared from a solution with a molar concentration of 1.3 M. With the aim of adapting the perovskite thickness to the diffusion length of the carriers, some tests were performed by reducing the molar concentration down to 1.2, 1.1, and 0.9 M and therefore the final thickness. This was tested for different perovskite compositions. In figure 4.12, the electrical performances of the $Cs_{0.05}FAPb(I_{0.3}Br_{0.7})_3$ are shown for different concentrations. The same tests were performed on other compositions. According to these plots, the best

results overall were reached for 1.3 M, and on average by the 0.9 M. This can be misleading since only few measurements were taken for the 0.9 M case and for FIRA processed batch of cells that showed the best performing 1.3 M.

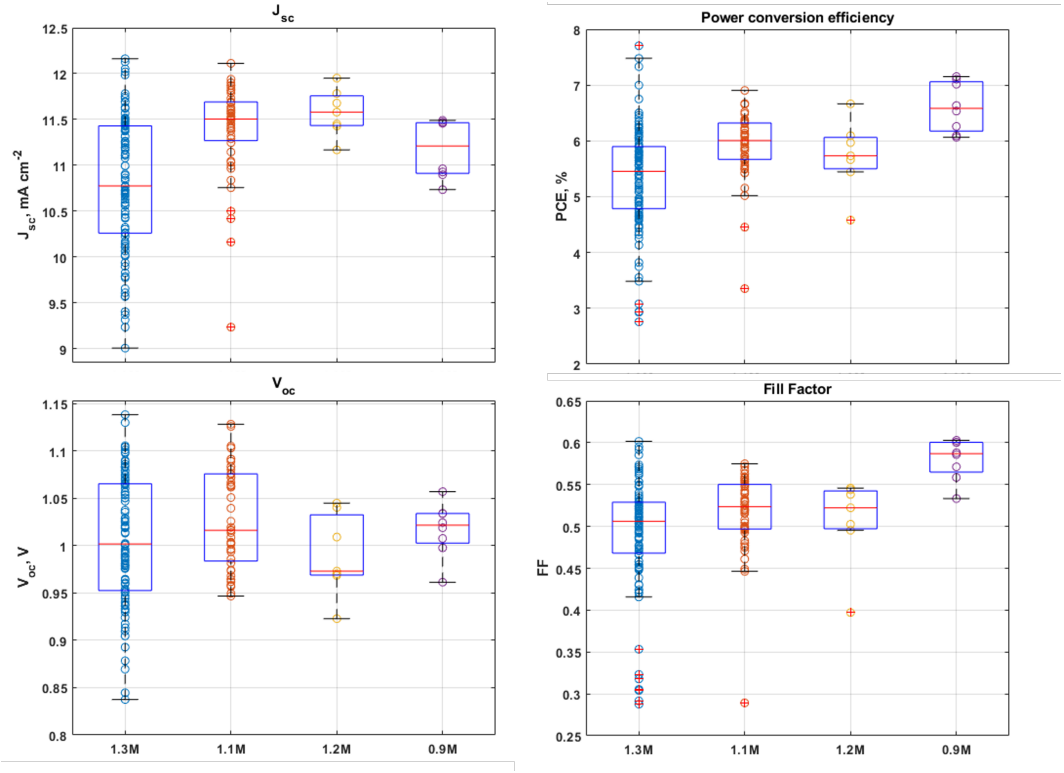

Figure 4.12. From the top left anticlockwise the short circuit current, open circuit voltage, fill factor, and power conversion efficiency for different molar concentrations of $Cs_{0.05}FA_{0.95}Pb(I_{0.3}Br_{0.7})_3$.

4.2 Hole extraction process optimization

Generally, a reliable hole transport material (HTM) for perovskite solar cells (PVSCs) is an amorphous material with good conductivity, morphological stability, and high glass transition temperature (T_g). The *glass transition temperature* is the temperature above which the thermoplastic material behave as viscous or rubbery solid and below which they behave as brittle, glass-like solid [21]. During this project, three HTM were tested on top of the perovskite layer: Spiro-OMeTAD, PTAA, and NiOx. In the following paragraphs, a description of these materials and the experimental results obtained are going to be presented and discussed.

4.2.1 PTAA as an alternative to Spiro-OMEtAD as HTL

The most efficient perovskite solar cells developed nowadays are based on Spiro-OMeTAD (2,2',7,7'-Tetrakis[N,N-di(4-methoxyphenyl)amino]-9,9'-spirobifluorene) as HTM. To improve its hole extraction properties, it is commonly doped with p-dopants as lithium bistrifluoromethanesulfonimidate (LiTFSI) and 4-tertbutylpyridine (tBP) which mainly improves morphology. Pristine spiro-OMeTAD shows a conductivity of 2.5×10^{-7} S cm^{-1} and up to 2×10^{-5} S cm^{-1} when doped with LiTFSI and tBP. One of the issues related to Spiro-OMeTAD is its relative low T_g. Indeed, It has been shown that it tends to degrade rapidly at temperatures as low as 85°C. Considering real environmental conditions, a stable perovskite solar cell has to be able to withstand temperatures up to this value. On the other hand, PTAA (Poly[bis(4-phenyl)(2,4,6-trimethylphenyl)amine), another widely explored HTM, was proved to be able to reach temperatures up to 300°C without showing glass transition or melting phase features. Pristine PTAA conductivity was determined to be 5.98×10^{-7} S cm^{-1} and up to 3.4×10^{-5} S cm^{-1} when doped with LiTFSI and tBP as for spiro-OMeTAD [68, 69]. During this thesis project, most of the solar cells were realized with spiro-OMeTAD (called sometimes *spiro* in the following) doped with LiTFSI and tBP as HTM. Given the above considerations, PTAA was tested as alternative HTM on some perovskite compositions.

In figure 4.13 are shown two SEM top view of two samples with spiro on top of the perovskite. The HTM shows an homogeneous coverage of the underlying rough perovskite layer. Indeed, spiro is know as a good material in terms of coverage of rough surfaces [69]. Sometimes, some high peaks cannot be covered as shown in 4.13b. These are cause of reduction of the electrical performances of the device. Good coverage can also be found in the PTAA samples. An example is visible in figure 4.14. This cross-section view allows to see how well PTAA follows the shape of the rough perovskite. In order to compare directly the performances of PTAA and spiro-OMeTAD, different solar cells were fabricated and their JV curve measured under sun simulator. In figure 4.15 are plotted the electrical performances of $Cs_{0.05}FA_{0.95}PbI_3$ samples having a PTAA as HTM. The concentration of the precursor solution composed by PTAA dissolved in chlorobenzene was varied from 5 to 35 mg/ml. This to tune the thickness of the final hole transport layer. The best performances were reached for a concentration of 15 mg/ml. Nevertheless, according to the results, the PTAA does not allow to reach the same numbers of Spiro-OMeTAD. Especially in terms of V_{oc} and PCE.

Few attempts of doping with tBP were made but without positive results.

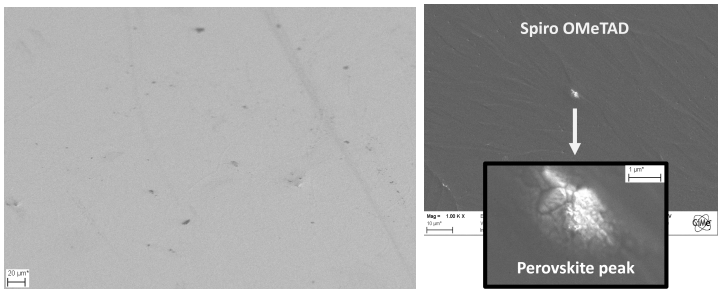

(a) **(b)**

Figure 4.13. SEM top view of Spiro-OMeTAD on perovskite **(a)** The spiro layer covers homogeneously the underlying perovskite. Scale 20 μm **(b)** A peak of perovskite through the HTL is highlighted. Scale 10 μm.

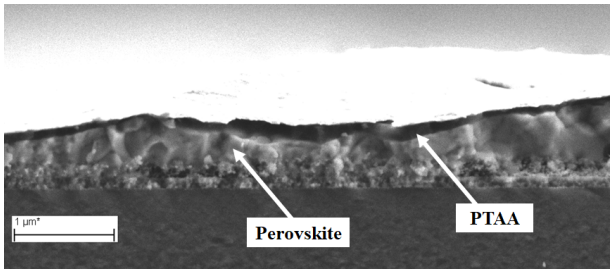

Figure 4.14. A SEM cross-section view of a PTAA on perovskite sample. Scale 1 μm.

Anode interfacial layer

Transition metal oxides (TMO) such as molybdenum trioxide (MoO_3), vanadium pentoxide (V_2O_5) or tungsten trioxide (WO_3) are widely studied because they behave as good charge injection and extraction materials when employed in organic electronic devices [70]. The first application of TMOs in organic electronics dates back to 1990's when Tokito et al. applied this technology to realize organic light emitting diodes (OLEDs) [71]. This class of materials behave as good hole-extraction layers and can be applied for this purpose also in organic photovoltaic. They behave as conducting p-type materials with values of workfunction around 7 eV. Indeed, to have good hole extraction layer, large workfunctions are required. Moreover, the oxygen vacancies present in these metal oxides build up a path that is exploited by the holes to leave the material and reach the electrode [70, 72].

Considering these studies, to enhance the hole extraction process and increase the performances of the solar devices, MoO_x was deposited through thermal evaporation on top of the HTL for some perovskite compositions. This material shows good performances as both hole-extraction layer and dielectric layer for a dielectric/metal/dielectric transparent electrode [73, 74]. Specifically, for this project it was mainly deposited on top of PTAA with the

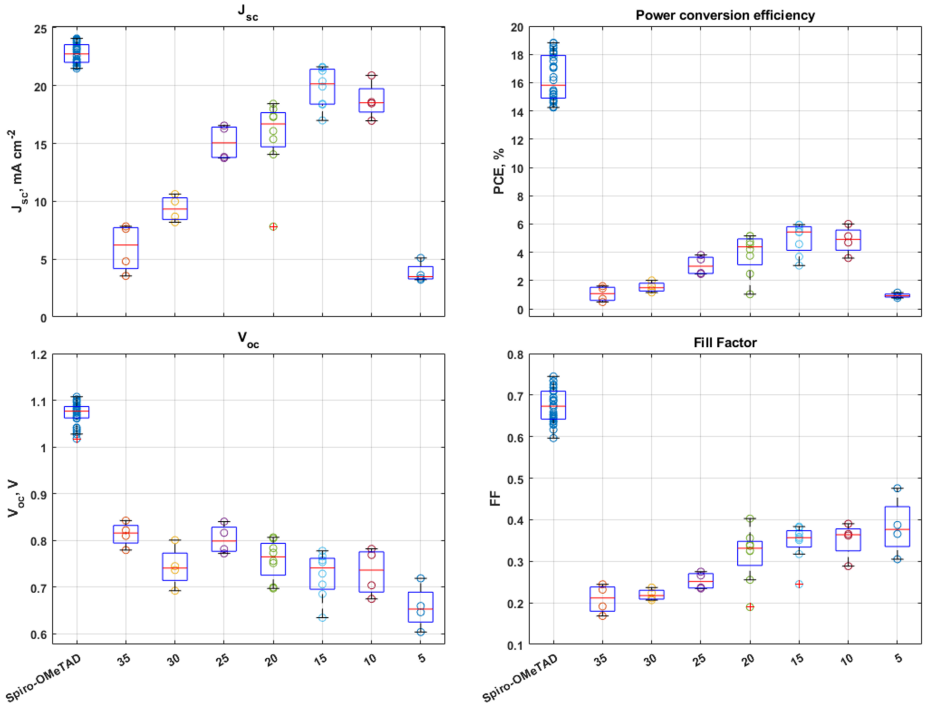

Figure 4.15. From the top left anticlockwise the short circuit current, open circuit voltage, fill factor, and power conversion efficiency for different molar concentrations (in mg/ml) of PTAA deposited on top of $Cs_{0.05}FA_{0.95}PbI_3$.

purpose to improve its performances as HTL. In figure 4.16 are shown the electrical performances for $Cs_{0.05}FA_{0.95}PbI_3$ perovskite devices having PTAA 15 mg/ml as HTL. The best results were reached for a MoO_x of thickness 2 nm. PCE values up to 13% are reached in some samples. By comparing these results with the ones in figure 4.15 where PTAA did not have any hole-extraction layer on top, it can be concluded that MoO_x lead to performances improvement. Moreover, being a transition metal oxide, it is a stable material that can act as a sort of encapsulant for the underlying organic materials sensitive to real environmental conditions. On the other hand, for the perovskite layers coated with Spiro-OMeTAD, only few tests were performed and none of them showed improvement.

4.2.2 Nickel (II) oxide as inorganic HTL

Nickel (II) oxide (NiO) is a inorganic p-type hole selective material. It is cheaper than the widely employed Spiro-OMeTAD and PTAA and is a stable material. Moreover acts as an incapsulant for the underlying perovskite layer. It can be deposited as e.g. nanoparticles through spin coating. But, in order to have performance comparable with the two previously mentioned HTL, its deposition methods must be optimized [75]. Some attempts were performed during the project on trying to deposit NiO on top of the perovskite layer, and substitute the organic HTL. The deposition technique available in the laboratory for NiO deposition was PVD RF sputtering. After few attempts of deposition, the performances of the devices were close to zero in terms of PCE. One hypothesis behind these results could be

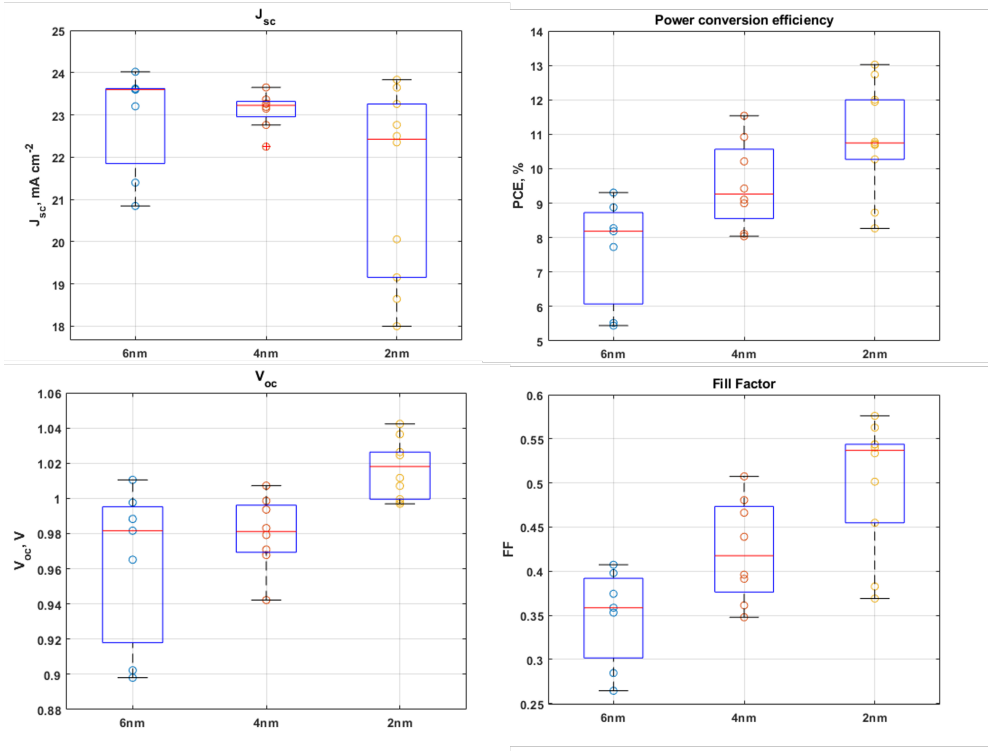

Figure 4.16. Results for a PTAA density of 15 mg/ml for different MoO_x thicknesses.

the deposition technique itself that damaged the perovskite layer. Indeed, sputtered NiO was proven to be working in p-i-n perovskite solar cells structures where the HTL is deposited on the transparent conductive oxide e.g. ITO (Indium Tin Oxide) [75]. But no optimal results can be found for sputtering on top of the organic perovskite. Few last attempts were performed by modifying the working paramenters of the sputtering facility. The standard program used for the NiO deposition called NiO-unif in summarized in the table in figure 4.17. With the idea of trying to reduce the stress on the perovskite layer, the plasma power was decreased down to 50 W for some conditions. The results for different thicknesses are visible in figure 4.17. Is is clear that no improvements were accomplished. Other tests as injecting oxygen in the chamber to enhance the quality of the NiO layer were tested. But these changes did not lead to any improvement.

4.3 Stability tests

One of the main issues that hinder the commercialization of perovskite solar cells is their instability under environmental conditions. Metal-halide perovskites are soluble in water and phase segregation phenomena arise after long term illumination. Therefore, humidity is harmful for perovskite stability, and encapsulation of the devices is needed for real applications [76]. After the development of the best wide bandgap perovskite compositions, a long term stability test was performed on some solar cells. In figure 4.18 is shown the PCE tracking for different perovskite compositions under light-soaking stability test ISOS-L-1 ([77]) but with relative humidity RH = 0% to simulate the encapsulation of the cell. This analysis

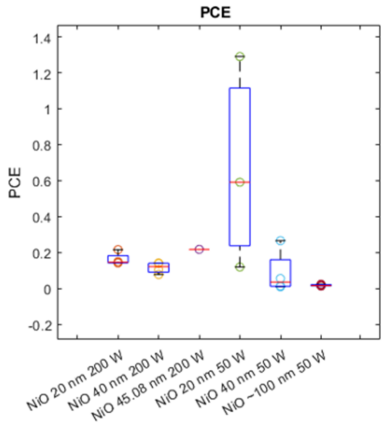

NiOx deposition parameters	NiO_unif values
Argon flux	30 sccm
Oxygen flux	0 sccm
Nitrogen flux	0 sccm
Pressure	8.0E-03 mbar
Source	RF
Plasma power	200 W
Deposition rate	1.4 Å/s

Figure 4.17. PCE for different NiO deposition conditions on top of $Cs_{0.05}FA_{0.95}PbI_3$. On the right, the standard deposition parameters for NiO

allows to separate the degradation due to light illumination from the one related to humidity exposure. The control samples seems to show a sudden drop during the first minutes of illumination, followed by a recovery during the same day. This can be better noticed by looking at the purple plot in 4.18a. Then the curves remain more or less stable along the successive days. The stability curves in figure 4.18b show different trend according to the perovskite composition. The Cl^--containing cells are characterized by a negligible initial drop. Indeed, their normalized plot is closer to PCE norm. 1 with respect to the control sample. The rich Br^- conditions suffered an initial drop too, followed by an increasing recovery along the next days. This could be the result of the photoactivation of some species with the time and/or the rearrangement the crystalline structure of the exposed films. Overall, the FIRA annealed samples show long term stable performances when exposed to light source only.

4.4 Design of dielectric/metal/dielectric transparent electrode

In order to allow the light transmitted by the wide-bandgap solar cell to reach the bottom cell, the electrode interfacing the HTL in a n-i-p configuration should be transparent to the lower energetic components of the spectrum. Therefore, the gold electrode employed for lab-scale experiments must be substituted with a semitransparent electrode to the near-IR range. In the AM1.5 spectrum of figure 4.19, two regions are highlighted. The one in blue is absorbed by the top cell (E_g = 2eV), while the one in red by the bottom cell (E_g = 1.55 eV). The wavelength range between 300 and 850 nm is essential in semi-transparent electrode studies. Indeed, one of the parameters usually employed to quantify the transmittance of the electrode is the Average Visible Transmittance (AVT) (see the methods chapter for its calculation). A good transparent electrode has to guarantee an high AVT. Together with the optical performances, a transparent electrode must be conductive too. Otherwise charge extraction would be hindered. According to theoretical results [74, 78, 79], an electrode that guarantees both high transmittance and conductivity is a MoO_x/Ag/MoO_x stack (sometimes called DMD stack in the following). The advantages related to the direct contact between the MoOx layer and the HTL have been already highlighted in the anode interface paragraph.

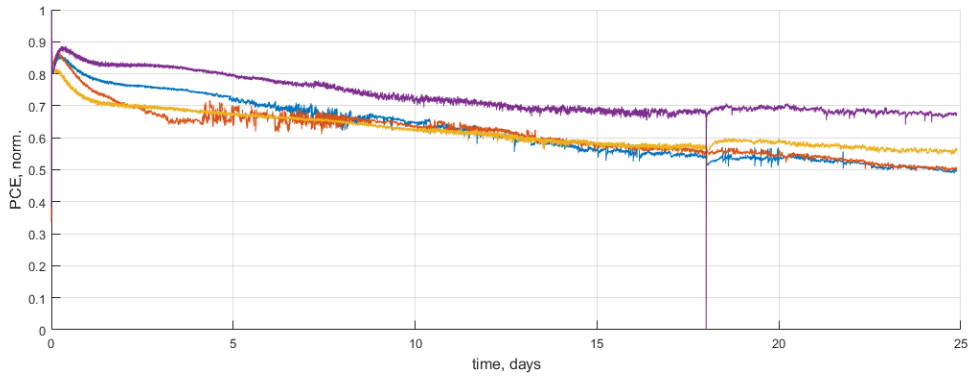

(a)

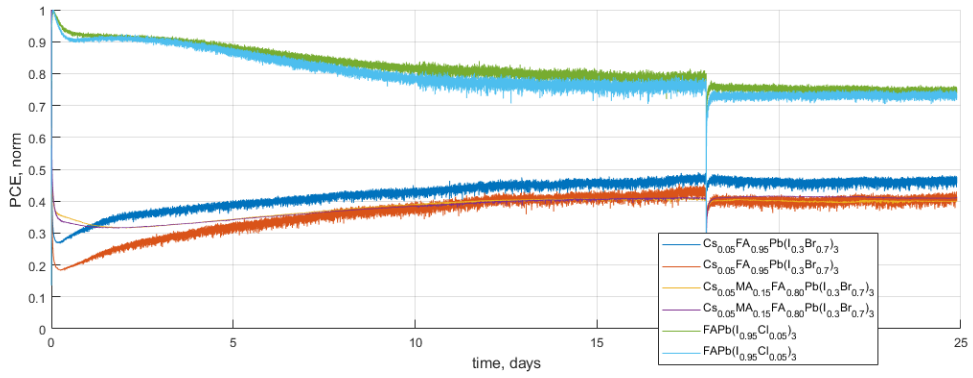

(b)

Figure 4.18. Power conversion efficiency tracking for a 25 days measurement. **(a)** Four control $Cs_{0.05}FA_{0.95}PbI_3$ cells under test. **(b)** Different wide bandgap conditions.

Moreover, MoOx would act as barrier from the ionic migration toward the organic HTM. From the results provided by [74] in figure 4.20b, the best AVT is reached for an Ag layer of 10 nm. About the dielectric layers, the best results from 4.20b taken from the experimental results of [78] are obtained for an inner layer (in contact with the HTL) thick 20 nm and an outer layer thick around 35 nm.

4.4.1 Electrical analysis

Silver, for thicknesses down to 10 nm tends to behave as a semiconductor due to the percolation threshold. Below this threshold, the high conductivity characteristics typical of silver tends to disappear. One explanation is related to the island growth that characterize silver [80]. Therefore, before testing the optical performances of the entire DMD stack, the electrical performances of thin films of silver were tested. In figure 4.21 are show the 4-probe measurement results for different Ag thickness on top of different MoO_x layers. According to the expectations, the lowest sheet resistances were obtained for thicker layer of silver. It can be noticed that by increasing the bottom MoO_x, on top of which Ag is grown, the electrical properties of silver increase. This can be attributed to nucleation-inducing properties of MoO_X [81]. Indeed, the thickness of MoO_x seems influencing more the 10 nm silver,

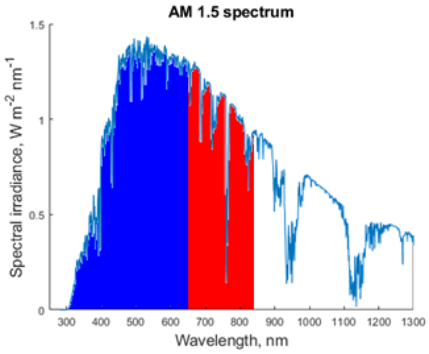

Figure 4.19. The AM1.5 spectrum. The blue region is the wavelength range absorbed by the top cell with a bandgap of 2 eV. While, the red one is absorbed by the bottom cell having a bandgap of 1.55 eV.

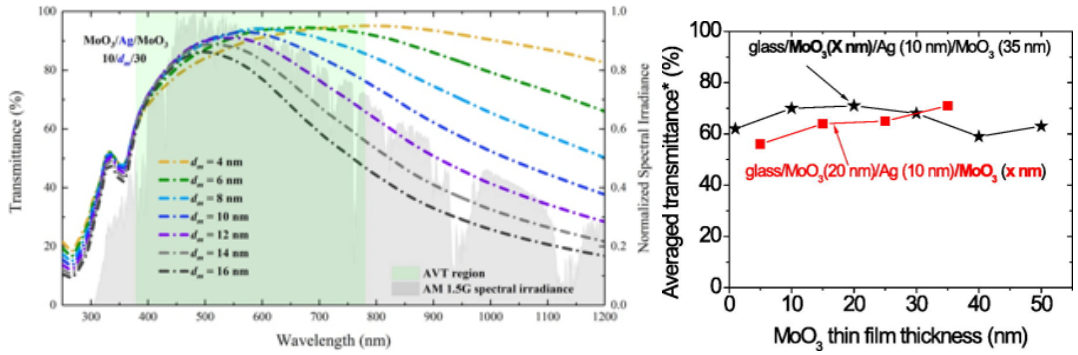

(a) **(b)**

Figure 4.20. **(a)** The transmittance trend with the Ag thickness according to [74] **(b)** The inner and outer MoO_x thickness influence on the AVT according to [78].

the more sensitive to the growth conditions. To further improve the Ag layer quality, two deposition rates were tested. No relevant differences can be noticed by tuning this process parameter. Unfortunately, these were the only results obtained from the experimental part of the DMD stack optimization. The last month of the project was planned for the optical optimization and the on-device deposition of the semitransparent stack. A lack of Nitrogen was experienced by the laboratory. Indeed this gas is essential for the functioning of the thermal evaporator, and no more molybdenum oxide depositions were allowed.

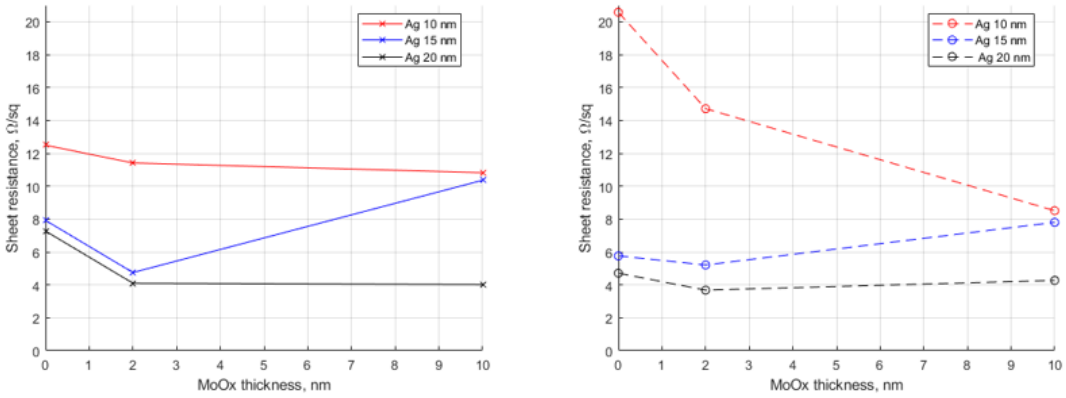

(a) **(b)**

Figure 4.21. Sheet resistance results for different Ag and bottom MoO_x layers. Each point is the average from three measurements. **(a)** Ag deposition rate 2.9 Å/s **(b)** Ag deposition rate 17.4 Å/s.

Conclusion and outlook

In the presented work, wide-bandgap perovskite solar cells were successfully developed with the novel Flash Infrared Annealing technique. Power conversion efficiencies over 7.5% and external quantum efficiency comparable with the high performance $Cs_{0.05}FA_{0.95}PbI_3$ were reached for the $Cs_{0.05}FA_{0.95}Pb(I_{0.3}Br_{0.7})_3$ perovskite. This result shows that FIRA processing can be successfully used to realize wide bandgap perovskite solar cells. The quality of the grown rich Br^- films looks comparable to the control ones. On the other hand, Cl^--containing solar cells with a pure FA^+ cation composition are less performing and several defects can be observed by imaging analyses. UV-Vis absorption and PL spectra confirm these results. Indeed, Cl^--containing films showed several excitonic levels and broad PL peaks, symptom of several defects and phase segregation along the thickness of the material. Further investigations are needed to understand the dynamics that lead small fractions of Cl^- to provoke a decrease of the film quality. In situ monitoring of the crystalline growth process during FIRA annealing can lead to a deeper understanding of the dynamics behind such different layer quality. Trying to improve Cl^--rich films by substituting FA^+ with Cs^+ and MA^+ is a path that must be investigated. Stability measurements, showed that FIRA grown perovskite samples can withstand long term solar illumination and, in some cases, it leads to the recovery of the initial performances. Structural analyses before and after the stability test could be exploited to understand the dynamics within the films.
PTAA as hole transport layer did not show any improvement with respect to the well established Spiro-OMeTAD. On the other hand, the addition of the MoO_x as hole-extraction enhancing layer did help with the improvement of the performances. Therefore, the introduction of metal oxides represents a viable solution to improve organic solar cells performances. The transparent electrode is an essential layer in tandem architectures, and the Dielectric/Metal/Dielectric stack has all the potentials to be successfully employed for this purpose thanks to its double role of anti reflective coating and electrode. The hole-enhancing properties of MoO_x combined with its protection for the underlying organic material makes it a good interfacial layer between the hole transport material and the metallic electrode. The silver as a metal in this stack showed good electrical performance despite close to the percolation threshold for 10 nm. The employed deposition technique play a main role on the final layer quality. Most of the researches show the optical performances of this stack but without applying it in real devices. Several experiments need to be performed to find an effective role of the DMD stack in photovoltaic applications.

Bibliography

[1] A. Thompson, B. Taylor, Guide for the use of the international system of units (si) (2008).

[2] I. E. Agency, Energy statistics manual, OECD Publishing, 2004.

[3] I. E. Agency, Energy statistics data browser, [Online]. URL: https://www.iea.org/data-and-statistics/data-tools/energy-statistics-data-browser (2022).

[4] U. N. F. C. on Climate Change (UNFCCC), The Paris agreement, UNFCCC, 2016.

[5] Our World in Data, "Global primary energy consumption by source" [Online]. URL: https://ourworldindata.org/energy-production-consumption, [Accessed: 11.2023].

[6] E. L. Wolf, Nanophysics of solar and renewable energy, John Wiley & Sons, 2012.

[7] I. E. Agency, Securing clean energy technology supply chains, [Online]. URL: https://iea.blob.core.windows.net/assets/0fe16228-521a-43d9-8da6-bbf08cc9f2b4/SecuringCleanEnergyTechnologySupplyChains.pdf (2022).

[8] I. R. E. Agency, I. E. A. P. P. Systems, End-of-life management: Solar photovoltaic panels (2016).

[9] S. Ananthakumar, J. R. Kumar, S. M. Babu, Third-generation solar cells: Concept, materials and performance-an overview, Emerging Nanostructured Materials for Energy and Environmental Science (2019) 305–339.

[10] H. Li, W. Zhang, Perovskite tandem solar cells: From fundamentals to commercial deployment, Chemical Reviews 120 (18) (2020) 9835–9950, pMID: 32786417.

[11] National Renewable Energy Laboratory (NREL), "Best Research-Cell Efficiency Chart" [Online]. URL: https://www.nrel.gov/pv/cell-efficiency.html, [Accessed: 11.2023].

[12] A. Polman, M. Knight, E. C. Garnett, B. Ehrler, W. C. Sinke, Photovoltaic materials: Present efficiencies and future challenges, Science 352 (6283) (2016) aad4424.

[13] S. Kasap, Optoelectronics & Photonics: Principles & Practices: International Edition, Pearson Education, 2013.

[14] A. S. Bati, Y. L. Zhong, P. L. Burn, M. K. Nazeeruddin, P. E. Shaw, M. Batmunkh, Next-generation applications for integrated perovskite solar cells, Communications Materials 4 (1) (2023) 2.

[15] PV Education [Online]. URL: https://www.pveducation.org/, [Accessed: 11.2023].

[16] P. Würfel, U. Würfel, Physics of solar cells: from basic principles to advanced concepts, John Wiley & Sons, 2016.

[17] B. Wardle, Principles and applications of photochemistry, John Wiley & Sons, 2009.

[18] G. Ghione, Semiconductor devices for high-speed optoelectronics, Vol. 116, Cambridge University Press Cambridge, 2009.

[19] E. Hecht, Optics, Pearson Education, Incorporated, 2017.

[20] J. Nelson, The Physics of Solar Cells, Series on Properties of Semiconductor Materials, Imperial College Press, 2003.

[21] W. Smith, J. Hashemi, F. Presuel-Moreno, Foundations of Materials Science and Engineering, McGraw-Hill Education, 2019.

[22] I. P. Herman, Optical diagnostics for thin film processing, Elsevier, 1996.

[23] K. Chondroudis, D. B. Mitzi, Electroluminescence from an organic−inorganic perovskite incorporating a quaterthiophene dye within lead halide perovskite layers, Chemistry of Materials 11 (11) (1999) 3028–3030.

[24] A. Kojima, K. Teshima, Y. Shirai, T. Miyasaka, Organometal halide perovskites as visible-light sensitizers for photovoltaic cells, Journal of the American Chemical Society 131 (17) (2009) 6050–6051, pMID: 19366264.

[25] S. Ahmad, S. Kazim, M. Grätzel, Perovskite Solar Cells: Materials, Processes, and Devices, John Wiley & Sons, 2022.

[26] D. B. Mitzi, Introduction: Perovskites, Chemical Reviews 119 (5) (2019) 3033–3035.

[27] M. A. Green, A. Ho-Baillie, H. J. Snaith, The emergence of perovskite solar cells, Nature photonics 8 (7) (2014) 506–514.

[28] K. D. Karlin, S. J. Lippard, Progress in inorganic chemistry, Vol. 54, Wiley Online Library, 2005.

[29] F. Ünlü, E. Jung, J. Haddad, A. Kulkarni, S. Öz, H. Choi, T. Fischer, S. Chakraborty, T. Kirchartz, S. Mathur, Understanding the interplay of stability and efficiency in a-site engineered lead halide perovskites, APL materials 8 (7) (2020).

[30] T. Chen, B. J. Foley, C. Park, C. M. Brown, L. W. Harriger, J. Lee, J. Ruff, M. Yoon, J. J. Choi, S.-H. Lee, Entropy-driven structural transition and kinetic trapping in formamidinium lead iodide perovskite, Science advances 2 (10) (2016) e1601650.

[31] S. P. Dunfield, L. Bliss, F. Zhang, J. M. Luther, K. Zhu, M. F. van Hest, M. O. Reese, J. J. Berry, From defects to degradation: A mechanistic understanding of degradation in perovskite solar cell devices and modules, Advanced Energy Materials 10 (26) (2020) 1904054.

[32] A. K. Jena, A. Kulkarni, T. Miyasaka, Halide perovskite photovoltaics: Background, status, and future prospects, Chemical Reviews 119 (5) (2019) 3036–3103.

[33] T. Leijtens, K. A. Bush, R. Prasanna, M. D. McGehee, Opportunities and challenges for tandem solar cells using metal halide perovskite semiconductors, Nature Energy 3 (10) (2018) 828–838.

[34] S. Sánchez, A. Hagfeldt, Flash infrared annealing for processing of perovskite solar cells, Perovskite Solar Cells: Materials, Processes, and Devices (2021) 33–89.

[35] S. Sanchez, X. Hua, N. Phung, U. Steiner, A. Abate, Flash infrared annealing for antisolvent-free highly efficient perovskite solar cells, Advanced Energy Materials 8 (12) (2018) 1702915.

[36] M. L. Terry, A. Straub, D. Inns, D. Song, A. G. Aberle, Large open-circuit voltage improvement by rapid thermal annealing of evaporated solid-phase-crystallized thin-film silicon solar cells on glass, Applied Physics Letters 86 (17) (2005).

[37] J. Troughton, M. J. Carnie, M. L. Davies, C. Charbonneau, E. H. Jewell, D. A. Worsley, T. M. Watson, Photonic flash-annealing of lead halide perovskite solar cells in 1 ms, Journal of Materials Chemistry A 4 (9) (2016) 3471–3476.

[38] S. Ghosh, S. Mishra, T. Singh, Antisolvents in perovskite solar cells: importance, issues, and alternatives, Advanced materials interfaces 7 (18) (2020) 2000950.

[39] H. Bhat, Introduction to crystal growth: principles and practice, CRC Press, 2014.

[40] H. Lüth, Solid surfaces, interfaces and thin films, Vol. 4, Springer, 2001.

[41] S. Sanchez, N. Christoph, B. Grobety, N. Phung, U. Steiner, M. Saliba, A. Abate, Efficient and stable inorganic perovskite solar cells manufactured by pulsed flash infrared annealing, Advanced Energy Materials 8 (30) (2018) 1802060.

[42] S. Sanchez, X. Hua, A. Gunzler, E. Bermudez-Urena, D. Septiadi, M. Saliba, U. Steiner, Flash infrared pulse time control of perovskite crystal nucleation and growth from solution, Crystal Growth & Design 20 (2) (2020) 670–679.

[43] P. Serafini, P. P. Boix, E. M. Barea, T. Edvinson, S. Sánchez, I. Mora-Seró, Photonic processing of mapbi3 films by flash annealing and rapid growth for high-performance perovskite solar cells, Solar Rrl 6 (12) (2022) 2200641.

[44] S. Sánchez, S. Cacovich, G. Vidon, J.-F. Guillemoles, F. Eickemeyer, S. M. Zakeeruddin, J. E. Schawe, J. F. Löffler, C. Cayron, P. Schouwink, et al., Thermally controlled growth of photoactive fapbi 3 films for highly stable perovskite solar cells, Energy & Environmental Science 15 (9) (2022) 3862–3876.

[45] S. Sánchez, L. Pfeifer, N. Vlachopoulos, A. Hagfeldt, Rapid hybrid perovskite film crystallization from solution, Chemical Society Reviews 50 (12) (2021) 7108–7131.

[46] S. Sánchez, M. Vallés-Pelarda, J.-A. Alberola-Borràs, R. Vidal, J. J. Jerónimo-Rendón, M. Saliba, P. P. Boix, I. Mora-Seró, Flash infrared annealing as a cost-effective and low environmental impact processing method for planar perovskite solar cells, Materials Today 31 (2019) 39–46.

[47] Ossila company, "UV Ozone treatment" [Online]. URL: `https://www.ossila.com/products/uv-ozone-cleaner`, [Accessed: 11.2023].

[48] A. R. West, Solid State Chemistry and its Applications, John Wiley & Sons, 2014.

[49] Center of MicroNanoTechnology, EPFL, "PVD definitions" [Online]. URL: `https://www.epfl.ch/research/facilities/cmi/process/thin-films/thin-films-definitions/`, [Accessed: 11.2023].

[50] Center of MicroNanoTechnology, EPFL, "Comelec C-30-S" [Online]. URL: `https://www.epfl.ch/research/facilities/cmi/equipment/thin-films/comelec-c-30-s/`, [Accessed: 11.2023].

[51] The Basics of UV-Vis Spectrophotometry, A primer, Agilent Technologies Inc., 2021.

[52] C. Yang, D. Liu, M. Bates, M. C. Barr, R. R. Lunt, How to accurately report transparent solar cells, Joule 3 (8) (2019) 1803–1809.

[53] Fluorolog-3, Operation Manual, Horiba Group, 2002.

[54] R. K. Leach, Good Practice Guide No. 37 - The Measurement of Surface Texture using Stylus Instruments, NPL-National Physical Laboratory, 2014.

[55] G. E. Eperon, S. D. Stranks, C. Menelaou, M. B. Johnston, L. M. Herz, H. J. Snaith, Formamidinium lead trihalide: a broadly tunable perovskite for efficient planar heterojunction solar cells, Energy & Environmental Science 7 (3) (2014) 982–988.

[56] D. Zhang, D. Li, Y. Hu, A. Mei, H. Han, Degradation pathways in perovskite solar cells and how to meet international standards, Communications Materials 3 (1) (2022) 58.

[57] L. Gránásy, T. Pusztai, G. Tegze, J. A. Warren, J. F. Douglas, Growth and form of spherulites, Physical Review E 72 (1) (2005) 011605.

[58] L. A. Muscarella, E. M. Hutter, F. Wittmann, Y. W. Woo, Y.-K. Jung, L. McGovern, J. Versluis, A. Walsh, H. J. Bakker, B. Ehrler, Lattice compression increases the activation barrier for phase segregation in mixed-halide perovskites, ACS energy letters 5 (10) (2020) 3152–3158.

[59] A. Rajagopal, Z. Yang, S. B. Jo, I. L. Braly, P.-W. Liang, H. W. Hillhouse, A. K.-Y. Jen, Highly efficient perovskite–perovskite tandem solar cells reaching 80% of the theoretical limit in photovoltage, Advanced materials 29 (34) (2017) 1702140.

[60] M. Abdi-Jalebi, M. I. Dar, A. Sadhanala, E. M. Johansson, M. Pazoki, Optical absorption and photoluminescence spectroscopy, in: Characterization Techniques for Perovskite Solar Cell Materials, Elsevier, 2020, pp. 49–79.

[61] T. Nie, Z. Fang, X. Ren, Y. Duan, S. Liu, Recent advances in wide-bandgap organic–inorganic halide perovskite solar cells and tandem application, Nano-Micro Letters 15 (1) (2023) 70.

[62] W. J. Jang, H. W. Jang, S. Y. Kim, Recent advances in wide bandgap perovskite solar cells: Focus on lead-free materials for tandem structures, Small Methods (2023) 2300207.

[63] A. Binek, F. C. Hanusch, P. Docampo, T. Bein, Stabilization of the trigonal high-temperature phase of formamidinium lead iodide, The journal of physical chemistry letters 6 (7) (2015) 1249–1253.

[64] B. Conings, J. Drijkoningen, N. Gauquelin, A. Babayigit, J. D'Haen, L. D'Olieslaeger, A. Ethirajan, J. Verbeeck, J. Manca, E. Mosconi, et al., Intrinsic thermal instability of methylammonium lead trihalide perovskite, Advanced Energy Materials 5 (15) (2015) 1500477.

[65] X. Shen, B. M. Gallant, P. Holzhey, J. A. Smith, K. A. Elmestekawy, Z. Yuan, P. Rathnayake, S. Bernardi, A. Dasgupta, E. Kasparavicius, et al., Chloride-based additive engineering for efficient and stable wide-bandgap perovskite solar cells, Advanced Materials (2023) 2211742.

[66] O. Shargaieva, L. Kuske, J. Rappich, E. Unger, N. H. Nickel, Building blocks of hybrid perovskites: A photoluminescence study of lead-iodide solution species, ChemPhysChem 21 (20) (2020) 2327–2333.

[67] S. J. Yoon, K. G. Stamplecoskie, P. V. Kamat, How lead halide complex chemistry dictates the composition of mixed halide perovskites, The journal of physical chemistry letters 7 (7) (2016) 1368–1373.

[68] F. M. Rombach, S. A. Haque, T. J. Macdonald, Lessons learned from spiro-ometad and ptaa in perovskite solar cells, Energy & Environmental Science 14 (10) (2021) 5161–5190.

[69] L. Nakka, Y. Cheng, A. G. Aberle, F. Lin, Analytical review of spiro-ometad hole transport materials: Paths toward stable and efficient perovskite solar cells, Advanced Energy and Sustainability Research 3 (8) (2022) 2200045.

[70] J. Meyer, S. Hamwi, M. Kröger, W. Kowalsky, T. Riedl, A. Kahn, Transition metal oxides for organic electronics: energetics, device physics and applications, Advanced materials 24 (40) (2012) 5408–5427.

[71] S. Tokito, K. Noda, Y. Taga, Metal oxides as a hole-injecting layer for an organic electroluminescent device, Journal of Physics D: Applied Physics 29 (11) (1996) 2750.

[72] L. Lin, C. Gu, J. Zhu, Q. Ye, E. Jiang, W. Wang, M. Liao, Z. Yang, Y. Zeng, J. Sheng, et al., Engineering of hole-selective contact for high-performance perovskite solar cell featuring silver back-electrode, Journal of Materials Science 54 (2019) 7789–7797.

[73] L. Chang, L. Duan, M. Sheng, J. Yuan, H. Yi, Y. Zou, A. Uddin, Optimising non-patterned moo3/ag/moo3 anode for high-performance semi-transparent organic solar cells towards window applications, Nanomaterials 10 (9) (2020).

[74] Ç. Çetinkaya, E. Çokduygulular, B. Kınacı, F. Güzelçimen, Y. Özen, H. İ. Efkere, İ. Candan, S. Emik, S. Özçelik, Design and fabrication of a semi-transparent solar cell considering the effect of the layer thickness of moo3/ag/moo3 transparent top contact on optical and electrical properties, Scientific Reports 11 (1) (2021) 13079.

[75] D. Di Girolamo, F. Di Giacomo, F. Matteocci, A. G. Marrani, D. Dini, A. Abate, Progress, highlights and perspectives on nio in perovskite photovoltaics, Chemical Science 11 (30) (2020) 7746–7759.

[76] H. Zhu, S. Teale, M. N. Lintangpradipto, S. Mahesh, B. Chen, M. D. McGehee, E. H. Sargent, O. M. Bakr, Long-term operating stability in perovskite photovoltaics, Nature Reviews Materials 8 (9) (2023) 569–586.

[77] M. V. Khenkin, E. A. Katz, A. Abate, G. Bardizza, J. J. Berry, C. Brabec, F. Brunetti, V. Bulović, Q. Burlingame, A. Di Carlo, et al., Consensus statement for stability assessment and reporting for perovskite photovoltaics based on isos procedures, Nature Energy 5 (1) (2020) 35–49.

[78] D.-T. Nguyen, S. Vedraine, L. Cattin, P. Torchio, M. Morsli, F. Flory, J. Bernède, Effect of the thickness of the moo3 layers on optical properties of moo3/ag/moo3 multilayer structures, Journal of Applied Physics 112 (6) (2012).

[79] C. Ji, D. Liu, C. Zhang, L. Jay Guo, Ultrathin-metal-film-based transparent electrodes with relative transmittance surpassing 100%, Nature communications 11 (1) (2020) 3367.

[80] A. Efros, B. I. Shklovskii, Critical behaviour of conductivity and dielectric constant near the metal-non-metal transition threshold, Physica status solidi (b) 76 (2) (1976) 475–485.

[81] Y. Xu, J. Wang, L. Sun, H. Huang, J. Han, H. Huang, L. Zhai, C. Zou, Top transparent electrodes for fabricating semitransparent organic and perovskite solar cells, Journal of Materials Chemistry C 9 (29) (2021) 9102–9123.